Orogenic gold in the Trans-Hudson orogen, Saskatchewan, Canada: Petrographic and geochemical insights from the Porky Lake system

Dixon, D.[1], Partin, C.A.[1*], Ansdell, K.[1], Voinot, A.[2], Ickert, R.B.[3]

[1]Department of Geological Sciences, University of Saskatchewan, 114 Science Place, Saskatoon, SK S7N 5E2, Canada

[2]Department of Geological Sciences and Geological Engineering, Queen's University, Bruce Wing/Miller Hall, 36 Union Street, Kingston, ON, K7L 3N6, Canada

[3]Department of Earth, Atmospheric, and Planetary Sciences, Purdue University, 550 Stadium Mall Drive, West Lafayette, IN, 47907-2051, United States

*Corresponding author: camille.partin@usask.ca

Dallas Dixon ORCID iD: 0009-0006-3930-2542

Abstract

Gold mineralization occurs within the Pine Lake greenstone belt in several known and prospective deposits in northern Saskatchewan, Canada. Systematics of gold mineralization at some locations within the Seabee Gold Operation, including the Porky Main and Porky West deposits, are poorly constrained but lie adjacent to the recently decommissioned Seabee mine, existing mill infrastructure, and active mining at the Santoy Mine Complex, enhancing their prospectivity. The Porky deposits are spatially associated with a shear zone separating mafic volcanic rocks (Assemblage A) from arenaceous metasedimentary rocks (Porky Lake Group) and are hosted in diverse rock types previously lacking petrographic and geochemical characterization. Gold mineralization is linked to calc-silicate alteration and occurs both in mafic volcanic rocks of Assemblage A and smoky quartz veins within the Porky Lake Group. To further assess the Porky deposits, mineralized drillcore samples were analyzed to determine the mineralogical and trace-element characteristics of sulfide-gold mineralization. Multiple sulfide generations are defined in a mineral paragenesis chart that outlines five sulfide phases (including pyrite), three of which are gold-bearing. These include sieve-textured Py3-Po2-Ccp2 ± Sp-Gn in pervasive calc-silicate alteration, oscillatory zoned Apy-Py4a/b-Po3-Ccp3 ± Ilm1 in smoky quartz veins, and remobilized Py6a/b with Au in fractures of earlier sulfide phases. Similar paragenetic features at the Santoy Mine and Fisher property support a belt-wide, multi-stage orogenic gold system. Finally, we report new geochronology for a ca. 1842 Ma granodiorite intruding the Porky Lake Group, refining previous age constraints.

Keywords: orogenic gold, Trans-Hudson orogen, greenstone belt, structurally-controlled mineral deposit, Paleoproterozoic

1 Introduction

Orogenic gold deposits are a critical source of gold globally (Goldfarb et al., 2001). These deposits typically form during the accretionary and collisional stages of orogenic belts and are hosted within greenstone belts, banded-iron formations, and turbidite sequences, where mineralization is associated with splays off crustal-scale structures with gold being deposited late- to post-peak metamorphism (Groves et al., 1998). Despite their recognized significance, the timing, fluid evolution, and sources of gold mineralization in orogenic gold deposits remain poorly constrained in many deposits worldwide. In some cases, these gold deposits have influence from intrusion-related deposits that are overprinted during orogenesis, such as the Wasamac deposit of the Abitibi greenstone belt, Quebec, Canada (Mériaud and Jébrak, 2017); early gold association with magmatic fluids during syn-volcanic plutonism where mineralization is subsequently upgraded by orogenesis (Meffre et al., 2016); and the interaction of magmatic-hydrothermal fluids during orogenesis, such as the Chalice deposit in the Yilgarn craton (Bucci et al., 2004). One approach to understanding the evolution and source of hydrothermal fluid sources is via the trace element composition of sulfide minerals associated with gold mineralization, such as pyrite and arsenopyrite, using laser ablation inductively coupled plasma mass spectrometry (LA-ICP-MS). This technique has been used to characterize gold deposits such as the Golden Ridge gold deposit, New Brunswick, Canada (Cardenas-Vera et al., 2023), the Huanxiangwa gold deposit, China (Gao et al., 2019), and the Chibougamau area, Quebec, Canada (Mathieu, 2019).

This study focuses on the Porky Lake deposits (named Porky West and Porky Main) that occur within the Reindeer zone of the Paleoproterozoic Trans-Hudson orogen (THO) in northern Saskatchewan, and are considered to be part of an orogenic gold system (Corrigan et al., 2007; Morelli and MacLachlan, 2012; Wood, 2016; Beaudin et al., 2024). The Reindeer zone represents the interior segment of the Trans-Hudson orogen (Stauffer, 1984; Ansdell, 2005; Fig. 1) and is known for hosting numerous orogenic gold and volcanogenic massive sulfide deposits, particularly in the Flin Flon and Glennie domains and the La Ronge-Lynn Lake belt (Corrigan et al., 2007; Morelli & MacLachlan, 2012). Orogenic gold deposits within the Reindeer zone are associated with the reactivation of older structures during Paleoproterozoic orogenesis (e.g., Lawley et al., 2020), including during late stages of terrane accretion, as suggested by ca. 1.83 to 1.72 Ga ages from gold deposits in the Flin Flon belt (e.g., Ansdell & Kyser, 1992; Rubingh et al., 2024). However, sulfide-gold associations and mineralization events within the Porky Lake system have not been characterized and their fluid characteristics are not known.

The Porky Lake deposits are part of the Seabee Gold Operation, which also includes the Santoy Mine Complex, the recently decommissioned Seabee mine, and the Fisher property. The deposits are hosted in various rock types of the Pine Lake greenstone belt and are typically associated with shear zones, such as the Santoy shear zone, that may have formed as secondary splays during the reactivation of regional structures, including the Tabbernor fault system (Delaney and Cutler, 1992; Durocher et al., 1992; Wood, 2016). Gold mineralization at Seabee, Santoy, and Fisher has been constrained to ca. 1780 to 1745 Ma. This interpretation is supported by multiple geochronological constraints, including Re-Os geochronology of gold-bearing pyrite from Fisher (1764.2 ± 5.6 Ma), U-Pb geochronology of titanite associated with gold-bearing calc-silicate alteration at Fisher (1755.5 ± 8.4 Ma), zircon U-Pb geochronology linked to calc-silicate alteration at Santoy (1754.0 ± 1.8 Ma), and Ar-Ar dating of biotite from the shear-hosted Seabee gold deposit (1769 ± 7 Ma; Schultz, 1996; Wood, 2016; Beaudin et al., 2024). This timing post-dates peak regional metamorphism of the Glennie domain that occurred at 1810 ± 10 Ma (Schneider et al., 2007). Unlike other deposits at the Seabee Gold Operation, which are dominantly hosted in volcanic-plutonic rocks, the Porky deposits are also hosted by metasedimentary rocks and associated shear zone that separates these rocks from the volcanic rocks of the area. The latter demonstrates the structural control of mineralization, which is consistent with other deposits in the belt.

This study provides the first detailed characterization of the Porky West and Porky Main deposits, including their mineral associations, relative age constraints, and stages of gold mineralization. Furthermore, this study provides a new geochronological constraint on the age of the Porky Lake Group, one of the host rocks to mineralization. An assessment of the trace element concentrations within sulfide mineral phases is presented to provide constraints on the evolution of the Porky Main and Porky West deposits, and the deposits of the Porky Lake system are compared to other gold deposits in the Seabee Gold Operation and within the Trans-Hudson orogen. Finally, mineralization stages for the Porky deposits are defined based on these data, which can provide insights into mineralization processes regionally within the Trans-Hudson orogen.

2 Geological Setting

2.1 Reindeer Zone of the Trans-Hudson Orogen

The Reindeer zone of the Paleoproterozoic Trans-Hudson orogen (Fig. 1) formed as a result of the collision of the Rae-Hearne, Sask, and Superior cratons as the Manikewan Ocean closed (Hoffman, 1988). It is composed of metamorphosed and deformed volcano-plutonic and sedimentary rocks, divided into lithostructural domains (Lewry et al., 1990). These domains can be grouped into intraoceanic volcanic-plutonic assemblages (Flin Flon and Glennie domains), juvenile crustal assemblages that were accreted to the Hearne craton (Wathaman/Chipewyan batholiths, Southern Indian Lake, Lynn Lake, La Ronge, and the Rottenstone domains), and the

Kisseynew domain, a presumed back-arc basin dominated by clastic sedimentary rocks (Ansdell, 2005; Corrigan et al., 2007).

The tectonic evolution of the Reindeer zone is related to the closure of the Manikewan Ocean (Corrigan et al., 2009). This was initiated during the formation of oceanic arcs between ca. 1.92 and 1.88 Ga (Stauffer, 1984; Syme and Bailes, 1993; Lucas et al., 1996; Ansdell, 2005; Corrigan et al., 2009). Intraoceanic accretion ca. 1.88–1.865 Ga led to the formation of the Flin Flon-Glennie Complex, a Paleoproterozoic volcanic-plutonic assemblage, and associated deformation (D_1) (Lewry et al., 1990; Lucas et al., 1996; Ashton, 1999). Andean-type continental arc formation, which included the Wathaman-Chipewyan batholith, occurred during subduction on the eastern Hearne margin ca. 1.865–1.845 Ga (Meyer et al., 1992), with continued successor arc magmatism persisting during early stages of collision (Van Schmus et al., 1987; Ansdell, 2005). During the collision of the Flin Flon-Glennie Complex with the La Ronge-Lynn Lake arc ca. 1.85–1.84 Ga (Zwanzig, 2000; Corrigan et al., 2005), deformation led to uplift and erosion, and the deposition of fluvial-alluvial sandstones of the Ourum, Porky Lake, Missi, and Wapawekka Lake groups in the Flin Flon-Glennie complex. The Sask craton subsequently collided with the Flin Flon-Glennie complex and generated the Pelican thrust, a structural zone that separates the overlying Glennie domain from the underlying Sask craton (Ashton et al., 2005). In the Kisseynew domain, deeper water facies sedimentation occurred in a back-arc basin preserved as the Burntwood Group (Ansdell et al., 1995; Ansdell, 2005; Corrigan et al., 2009). The last vestiges of the Manikewan Ocean closed at ca. 1.83–1.80 Ga, during the collision between the Superior craton, Reindeer zone, and Rae-Hearne craton (Lewry and Collerson, 1990), leading to the cessation of successor arc plutonism ca. 1.83–1.825 Ga (Van Schmus et al., 1987; Ansdell, 2005; Corrigan et al., 2009). During this time, widespread D_2 deformation coincided with peak metamorphism with resulting greenschist and amphibolite facies at 1810 ± 10 Ma (Lewry and Collerson, 1990; Schneider et al., 2007). Late- to post-collisional D_3 deformation (ca. < 1.80 Ga) involved brittle reactivation of the structures, such as the Tabbernor fault and associated splays. Subsequent D_4 brittle deformation occurred as regional folding and localized reactivation of earlier structures (Lewry et al., 1990; Wood, 2016). Lastly, the emplacement of late- to post-tectonic granites and pegmatites occurred ca. 1.770–1.762 Ga (Bickford et al., 1987; Chiarenzelli, 1989).

2.2 Geology of the Pine Lake Greenstone Belt

The Pine Lake greenstone belt of the Glennie domain comprises three supracrustal assemblages: the volcanic rock-dominated Assemblage A and Assemblage B, and the siliciclastic Porky Lake Group (Fig. 2). Assemblage A consists of metamorphosed mafic and felsic volcanic, subvolcanic intrusive, volcaniclastic, and minor siliciclastic rocks deposited between ca. 1886 and 1870 Ma (Delaney and Cutler, 1992; Durocher et al., 2001; Witvoet, 2023). Minor conglomerate, feldspar porphyry flows, pelite, feldspathic arenite, and mica schist are also present (Delaney, 1987). This assemblage is intruded by the 1879 ± 1.3 Ma gabbro and diorite-bearing Laonil Lake intrusive complex and the 1884 ± 1.3 Ma gabbroic Eisler Lake intrusive suite (Witvoet, 2023). Assemblage B is composed of felsic and hornblende-bearing volcanoclastic rocks, lapilli tuff, chlorite-actinolite schist, and a basal polymictic conglomerate that marks the unconformity surface above the older Assemblage A (Delaney and Cutler, 1992). The depositional age of Assemblage B is constrained by rhyolite intercalated within the basal Pine Lake conglomerate yielding a U-Pb zircon age of 1838 ± 2 Ma (McNicoll et al., 1992). The Porky Lake Group occurs as micaceous arkosic rocks preserving trough crossbedding (in strain shadows) with pebble-sized granitic and heterolithic conglomerate beds (Delaney, 1986). Gold mineralization of the Porky Lake deposits occurs in both altered mafic volcanic rocks of Assemblage A and the Porky Lake Group (Fig. 3B).

There are no published age constraints directly from the Porky Lake Group. Furthermore, both Assemblage A and the Porky Lake Group are intruded by an undated granodiorite. Although an unconformity surface has never been directly observed, Lewry (1977) described the contact between Assemblage A and the Porky Lake Group as being highly modified by strain during later deformation and that the surface between the volcanic rocks and sedimentary rocks possibly represents an unconformity (Fig. 3C).

During early structural mapping of the Glennie domain, Lewry (1977) defined three episodes of deformation. Subsequent regional mapping conducted by Lewry et al. (1990) and Ashton et al. (2005) led to the recognition of several km-scale thrust sheets bounded by high strain zones. At a regional scale, D_1 involved two phases of isoclinal recumbent folding (F_1) associated with southwest-directed thrusting during intra-oceanic accretion. Ductile D_2 deformation occurred during the convergence of the Hearne, Sask, and Superior cratons ca. 1840–1800 Ma and was responsible for east-west trending F_2 folds, transposed regional S_2 foliation ($S_0/_1/_2$), and shear zones and domain-bounding high-strain zones (Lewry et al., 1990; McEwan, 2013; Wood, 2016). Metamorphism associated with D_2 attained temperatures and pressures around 500–650º C and 2.5–7 kbar (Durocher, 1997), with peak metamorphism of the region at 1810 ± 10 Ma with subsequent uplift and cooling (Schneider et al., 2007). Diachronous metamorphism can occur at different crustal levels, however, and younger ages obtained within the Glennie domain show a retrograde path brought on by rapid uplift and cooling that occurred ca. 1770 Ma (Schneider et al., 2007). Peak metamorphism of the study area is recorded by multiple monazite growth events between ca. 1801 and 1777 Ma, and zircon metamorphic rims forming at 1805 ± 3.5 Ma (Schneider et al., 2007). In addition, Wood (2016) reports a zircon U-Pb age of 1807 ± 7 Ma for the Packman Lake pluton, which intrudes Assemblage A rocks south of the Santoy Mine Complex, and is interpreted to be a collisional granite that formed during peak metamorphism. D_3 involved late to post-collisional deformation (ca. 1800–1735 Ma) and resulted in the development of the regional north-northwest plunging folds of the Ray Lake and Carruthers Lake synform and antiform and transposed axial planar foliation S_3, Type 2 and 3 interference folds (F_{2-3}), and dextral-reverse oblique-slip and later sinistral strike-slip of the Tabbernor fault system (Elliot, 1995; Wood, 2016). The Porky Lake Group is in structural contact with Assemblage A along a late D_2 shear zone, and occurs within the core of the D_3 Ray Lake synform (Delaney, 2016; SRK Consulting, 2021).

3 Methods

3.1 Sample Collection

Samples were collected from 27 drillholes, with a total of 153 samples taken at depths ranging from 1.45 to 158.30 meters along the length of the drillholes. In addition, 17 samples were collected from existing outcrop channels cut in 2021 from the Porky Main area. The selection of samples was based on various criteria, including rock types, cross-cutting relationships, and the presence of visible gold, sulfide minerals, quartz veins, and alteration. A granodiorite that intrudes the Porky Lake Group was sampled for U-Pb geochronology (Fig. 3).

3.2 Petrographic Analysis

Mineral assemblages and textural relationships were identified to construct a paragenetic sequence for the Porky Main and Porky West deposits. From the 153 core samples collected, 53 polished thin sections were prepared at the University of Saskatchewan Thin Section Laboratory and Precision Petrographics Ltd., targeting samples that exhibit key relationships between veins, alteration, mineralization, and the host rocks. Five channel samples were also cut into billets for thin sections and selected based on various rock types and gold grades. The thin sections were examined using a Meiji Techno MT9930 microscope with an Infinity1 camera attachment. Mineral abbreviations used are those of Whitney and Evans (2010).

3.3 Electron Microprobe Analyses

After petrographic study, 22 thin sections were chosen for electron microprobe analysis at the Microbeam and Image Analysis Facility at the University of Manitoba, Canada. The thin sections were cleaned to remove contaminants, carbon-coated, and then analyzed using a CAMECA SX100 electron microprobe. Five wavelength-dispersive spectrometers were employed to quantify knowals, and an energy-dispersive spectrometer was used with the Peak Sight analysis software to identify unknown minerals. The microprobe was configured with an accelerating voltage of 20 kV for sulfide minerals and 15 kV for silicates and oxides, a beam current of 20 nA, and a diameter between 1 and 10 microns. X-ray conditions are described in Supplementary Data File A. X-ray intensities were standardized using natural standards in silicates, synthetic phosphates for rare earth elements in apatite, and synthetic and pure metals in sulfide and BiTe mineral phases. The Pouchou & Pichoir (1984) matrix correction scheme, which includes ZAF (Atomic Number, Absorption, and Fluorescence) corrections, was applied to all analyzed phases using the X-ray form factor, attenuation, and scattering (FFAST) mass absorption coefficient table (Chantler, 2000).

3.4 Laser Ablation Inductively Coupled Plasma Mass Spectrometry

Following electron microprobe work, 13 thin sections were chosen from the Porky Main and Porky West deposits for semi-quantitative laser ablation inductively coupled plasma mass spectrometry (LA-ICP-MS) analyses. Samples were selected based on the presence of visible and presumed refractory gold, as indicated by assay data, and the presence of different sulfide mineral generations and calc-silicate alteration. The goal was to identify trace elements, including gold, and their distribution in sulfide minerals (pyrite, pyrrhotite, arsenopyrite, and chalcopyrite) to differentiate mineral growth stages. The LA-ICP-MS analyses were conducted using an ESI-NWR Excimer 193nm ArF laser ablation system at the Queen's Facility for Isotope Research at Queen's University, Canada. The parameters used for the analyses included a beam size of 15 µm for coarse-grained sulfide minerals and 10 µm for fine-grained colloform sulfide minerals, and a laser frequency of 10 Hz. Between each line analysis, a 5 s recharge time was used with a 20 s washout time. Data were processed using Iolite v4 with a baseline reverse trim of 17 s and a baseline duration of 11 s. A NIST612 standard was employed to tune the instrument for maximum signal sensitivity to minimize oxides (<0.8%) and reduce a double charge effect (<5%). Additional certified reference standards included GSC-1G, GSD-1G, GSE-1G, CCu1e, FeS4, and FeS5. All standard lines were run for approximately 30 s. The GSC/D/E samples are USGS reference materials and consist of a fused glass of basaltic composition. The CCu1e, FeS4, and FeS5 standards are compressed pellets from Chicoutimi, Quebec. A total of 19 maps were generated from the thin sections. Each standard was run three times before and after each map area for increased QAQC and to correct for instrumental drift.

3.5 U-Pb Geochronology

A granodiorite unit that occurs along the contact between the Assemblage A mafic volcanic rock and the Porky Lake Group, and cross-cuts the arkosic unit in outcrop and drillcore, was sampled for U-Pb geochronology to constrain the age of the Porky Lake Group. The drillcore sample was sent to Zirchron LLC in Tucson, Arizona, for mineral separation using an electropulse disaggregator. Heavy minerals including zircon grains were further separated using standard procedures. At the University of Saskatchewan, zircon grains were chosen based on their crystal morphology, color and transparency, and overall appearance (i.e., free of fractures, alteration, inclusions, and overgrowth). The hand-picked, best-quality zircon grains were sent to Purdue University, Indiana, for chemical abrasion isotope dilution thermal ionization mass spectrometry (ID-TIMS). Zircon grains were first annealed in a muffle furnace at 900°C for 60 hours followed by partial dissolution in 24 mol/L HF and 1 mol/L HNO_3 while being held at 210°C for 10 hours in a steel jacketed polytetrafluoroethylene (PTFE) digestion vessel. Following the partial dissolution of zircon grains in HF and HNO_3 during chemical abrasion, 17 zircon fractions remained for the granodiorite. Grains that remained undissolved were then rinsed and cleaned by refluxing for several days in 7 mol/L HCl and mixed with 5–9 mg of the ^{205}Pb-^{233}U-^{235}U tracer ET535 (Condon et al., 2015; McLean et al., 2015). The grains were then dissolved, and Pb and U were separated by ion chromatography (Krogh, 1973). Both Pb and U were measured on a PhoeniX thermal ionization mass spectrometer.

4 Results

4.1 Representative Lithologies

The main rock types observed in the drillcore, of Porky West include subarkose and mafic volcanic rocks, with subordinate pegmatite and conglomerate units. In contrast, the rocks at Porky Main are, in order of abundance: subarkose arenite, mafic volcanic rocks, granodiorite, quartz diorite, intermediate volcanic rocks, and pegmatitic rocks with a subordinate wacke unit in the subarkose. These units were also observed near the deposits in outcrop (Fig. 3A; 4A–F). Porky Main and Porky West exhibit pervasive calc-silicate alteration and two sets of veins. Gold mineralization is associated with veins containing smoky quartz (Fig. 5A–C). The prefix "meta-" has been removed as all the rocks in this area have been subjected to amphibolite facies metamorphism with the exception of the pegmatite intrusions.

4.1.1 Assemblage A

4.1.1.1 Mafic Volcanic Unit

Aphanitic mafic volcanic rocks (basalt) are located south of the sheared contact with the Porky Group (Fig. 4A), and are dominated by hornblende (~50–55%), with quartz (15–20%), plagioclase feldspar (10–15%), biotite (8%), and trace amounts of magnetite and pyrrhotite (Fig. 6A). The altered mafic volcanic rock proximal to the shear zone has cm-scale bands of epidote-carbonate-diopside alteration with local silicification and chlorite alteration.

4.1.1.2 Intermediate Volcanic Unit

The intermediate volcanic rocks (dacite; Fig. 4B) are fine-grained and contain less hornblende and more plagioclase than the mafic volcanic rocks: they consist of hornblende (30–35%), plagioclase (25–30%), biotite (15–20%), quartz (20–30%), and trace amounts of magnetite and pyrrhotite (Fig. 6B). These units are moderately to strongly foliated, with strain increasing proximal to the shear zone with the fabric (S_2) defined by the alignment of biotite and hornblende.

4.1.2 Porky Lake Group

4.1.2.1 Subarkosic Sandstone Unit

The dominant unit of the Porky Lake Group is a fine-grained subarkosic sandstone (Fig. 4C–D) that consists of quartz (50–75%) with a granoblastic polygonal texture, muscovite (3–15%), biotite (5–15%), plagioclase feldspar (5–9%) with mild alteration to sericite (Fig. 6C–D), and trace pyrrhotite.

4.1.2.2 Conglomerate Unit

The conglomerate unit of the Porky Lake area occurs interbedded in the subarkosic unit: it consists predominantly of felsic, pebble-sized clasts with minor mafic clasts and is less abundant at Porky Main than Porky West (Fig. 4C). In areas where the clasts occur, they have been elongated in the direction of foliation and vary in abundance between 5 and 70%. The plagioclase shows a moderate degree of sericitization (Fig. 6C). The matrix of the conglomerate consists of plagioclase (30–45%), quartz (30–40%), muscovite (3–9%), biotite (1–5%), pyrrhotite (1–5%), and magnetite (1–5%).

4.1.2.3 Feldspathic Wacke Unit

A rare but distinctive feldspathic wacke unit occurs interbedded within the subarkosic units and close to the contact with Assemblage A. It is composed of fibrolitic sillimanite (25%), garnet (20%), biotite (15%), plagioclase (15%) with weak sericitic alteration, quartz (15%), muscovite (3%), ilmenite (5%), and pyrrhotite (2%) (Fig. 6E–F).

4.1.3 Intrusive Rocks

4.1.3.1 Granodiorite Unit The granodiorite is porphyritic with larger feldspar grains in a broadly equigranular groundmass with polygonal quartz. The rock consists of minor to moderate sericitization of plagioclase feldspar (30–45%), quartz (30–40%), muscovite (3–15%), biotite (3–15%), orthoclase (10–15%), pyrite (1–2%), and magnetite (1–2%) (Fig. 6G). This unit intrudes the mafic volcanic unit (Fig. 4E) and the Porky Lake Group (Fig. 3). It is commonly found along the contact between both units in drillcore in the Porky Main area. The granodiorite contains the S_2 foliation, which supports our interpretation that the intrusion pre-dates D_2/peak metamorphism.

4.1.3.2 Quartz Diorite Unit

The quartz dioriteis more coarse-grained than the more abundant granodiorite unit, and consists of plagioclase feldspar (35–40%), quartz (15–20%), biotite (15–29%), muscovite (2–15%), and magnetite (2–3%), with trace pyrite (Fig. 6H). The feldspar shows a low degree of sericitization. Due to the increased grain size, foliation fabric is not well-preserved but is still evident from the alignment of biotite. This unit was observed intruding the Porky Lake Group at the Porky Main deposit.

4.1.3.3 Pegmatite Unit

The pegmatite units occur in both Porky Main and Porky West areas but are more frequent in the latter and are found cutting the Porky Lake Group (Fig. 4F). The most abundant pegmatite consists of K-feldspar (35–50%) with varying degrees of alteration into sericite, euhedral muscovite (1–35%), quartz (20–45%), and garnet (4–25%) that are < 0.5 mm in size (Fig. 6I). K-feldspar and quartz commonly interlock at a triple point junction and are typically 2–4.5 mm in size. The plagioclase-rich pegmatite is dominated by plagioclase grains often > 3 mm and various degrees of alteration into sericite (35–50%), quartz (20–45%), garnet (4–6%), and muscovite (1–3%).

4.1.4 Alteration and Veins

The most prevalent veins (V_1) observed at the Porky Main and Porky West deposits occur in the volcanic units (Fig. 5A) and are composed of 40–60% quartz that forms triple points, albite (25–40%) with a low degree of alteration, diopside (15–25%), and K-feldspar (<5%) (Fig. 6J). Trace chalcopyrite, pyrite, pyrrhotite, and magnetite were observed and frequently occur together (Fig. 7A). These veins are typically thin (0.2 mm to 3 cm), semi-concordant and concordant to foliation, and commonly rimmed with diopside and calcite. These veins are likely synchronous with the calc-silicate alteration since they often form the core of the pervasive calc-silicate alteration. Visible gold was not observed with this vein generation.

The pervasive calc-silicate alteration of the Porky deposits occurs in the Assemblage A mafic volcanic unit (Fig. 5B) and is commonly associated with the V_1 veins. The alteration consists of subhedral diopside (~50%), albite (15%), quartz (25%), sericite (10%), pyrrhotite (±4–8%), pyrite

(±1–2%), chalcopyrite (±1–2%), sphalerite (±0–1%), and trace gold and galena (Fig. 6K, 7C). In thin section, quartz grains commonly form a triple point with undulose extinction and have a granoblastic amoeboid texture and irregular grain boundaries. Foliation is primarily defined by diopside.

The second generation of veins (V_2) observed are defined by smoky quartz veins (Fig. 5C) found in all Porky Main and Porky West lithologies but most abundant in the Porky Lake Group (Fig. 4D). The V_2 vein generation is interpreted to succeed the V_1 vein generation because V_1 veins are not found in the Porky Lake Group. However, V_2 is not observed to cross-cut V_1. In outcrop, quartz veins are transposed, boudinaged, and folded, indicating that the veins were emplaced prior to or during the early stages of D_2 deformation and subsequently modified during continued deformation. i These veins range in size from several cm to m, are mappable units in drillcore, and commonly contain significant gold mineralization. These veins consist of mosaic-textured quartz grains (>70–90%) with irregular grain boundaries that are commonly associated with subhedral to euhedral biotite (3–5%) that often occurs along quartz grain boundaries and along vein margins, chlorite (1–2%), K-feldspar (±1–2%), arsenopyrite (±3–8%), pyrite (±2–6%), pyrrhotite (±1–2), and chalcopyrite (±1–2) with trace gold (Fig. 6L). K-feldspar grains are commonly > 2 cm and are more abundant towards the rim of the veins. These veins are semi-concordant to concordant to foliation and often have variable diopside-actinolite-altered wall rock fragments when found in mafic volcanic units. Given the occurrence of visible gold, these veins and their associated sulfide minerals are the primary focus of this study.

4.2 Sulfide Mineral Generations, Gold, and Paragenetic Relationships

The primary sulfide minerals observed at the Porky Main and Porky West deposits include pyrite (Py), pyrrhotite (Po), chalcopyrite (Ccp), and arsenopyrite (Apy). Observations of primary sulfide minerals were used to generate a paragenetic sequence based on textural features, deformation, and the primary rock unit in which they occur. Pyrite was identified in six distinct phases across various lithologies. The first phase, Py1, is associated with calcareous V_1 veins and is typically anhedral to subhedral and contains few inclusions (Fig. 7A). Trace Py2 occurs in the sedimentary units, exhibiting a colloform texture and commonly showing significant dissolution and often found in close association with Py4a (Fig. 7B). Py3 is present in the calc-silicate alteration with Po2/Ccp2/Sp (Fig. 7C); these sieve-textured sulfide minerals are characterized by small, anhedral, and porous grains, often containing calcite inclusions. In V_2 veins, larger euhedral grains of Py4a are observed, frequently recrystallized, and contain inclusions of chalcopyrite and galena. Py4b, also found in the V_2 veins, forms a disseminated matrix surrounding the larger euhedral grains (Fig. 7D). Apy is also associated with these V_2 veins (Fig. 7E–F). Py5 is primarily found in the granodiorite and diorite units as small euhedral cubes in the foliation and is associated with peak metamorphism. Py6a results from remobilization and forms around brecciated quartz, biotite, and muscovite grains (Fig. 7G), while Py6b represents crystal lattice controlled exsolution with subparallel horizontal bands or relict zoning of earlier Py4a. (Fig. 7H). The phases associated with gold mineralization are Py3 through Py4a/b.

Pyrrhotite was similarly categorized into four generations. Po1 is not common, but it is anhedral and forms within V_1 veins. This sulfide generation occurs with Py1-Ccp1-Mag1. In the calc-silicate alteration, Po2 occurs as sieve-textured, anhedral grains with frequent calcite inclusions with Py3-Ccp2-Sp-Gn (Fig. 7C). Po3 is found in V_2 veins as larger anhedral grains surrounding the euhedral Py4a with associated Py4b-Ccp3. Lastly, Po4 forms small, anhedral grains aligned with foliation, predominantly observed in the volcanic and sedimentary units. This generation is synchronous with Py5, which occurs in the intrusive units, and Ilm2, which is commonly aligned with foliation.

Chalcopyrite is present in three distinct forms. Ccp1 is observed in V_1 veins as small, anhedral grains with Po1-Py1-Mag1 and is not abundant (Fig. 7A). In the calc-silicate alteration, Ccp2 is coarser, anhedral, and highly porous, with inclusions such as calcite and a Po2-Sp association (Fig. 7C). Ccp3 occurs as dissemination in V_2 veins with Py4b-Po3 around larger euhedral Py4a (Fig. 7D).

Arsenopyrite is primarily associated with V_2 veins, where the anhedral grains are commonly larger than 4 mm, appear to have been partially dissolved, and are rich in inclusions including chalcopyrite, pyrite, and pyrrhotite (Fig. 7E-F). These sulfide minerals are rarely associated with Py4a despite forming in the V_2 veins.

The albite-diopside V_1 veins of the mafic volcanic unit contain trace Py1-Po1-Ccp1, all of which are anhedral. Py2 is a colloform pyrite which is partially dissolved and is observed in the subarkose arenite, and likely formed prior to the main mineralization events. In contrast, the mafic volcanic rock that had been affected by calc-silicate alteration contains abundant Py3-Po2-Ccp2-Gn-Sp. Sulfide minerals of the smoky quartz V_2 veins are often recrystallized with Ccp and Gn micro-inclusions, with Py4a often being euhedral and > 4 mm. Py4a is commonly associated with a fine-grained, anhedral, disseminated Py4b-Ccp3-Po3 matrix around the larger euhedral grain. These veins are often associated with Apy-Ilm1-Tbi2. A pegmatite unit that has been altered by these veins is associated with Apy and Ccp3, and unaltered samples were not observed with sulfide minerals. This suggests that the V_2 generation are the primary source of gold and sulfide mineralization in the system. Py5/Po4, which are small, anhedral, and aligned to foliation, were observed in all unaltered rock units (Fig. 6G). Lastly, Py6a/b is associated with brittle deformation.

Using the above sulfide mineral generations, a paragenesis sequence (Fig. 8) was created, and subdivided based on host rock and the relative timing of events (i.e., alteration, veins, and relationship to peak metamorphism and associated foliation).

Three forms of gold were observed. The earliest gold, Au1, occurs in the calc-silicate alteration (Fig. 9A). These grains are < 0.5 mm in size, have irregular and varying shapes with jagged edges, and contain Ag (8.68–10.37 wt%), Hg (2.35–2.81 wt%), and Bi (0.57–0.59 wt% (Supplementary Data File A). These gold grains show a shared grain boundary with galena and commonly occur with Tbi1. Au2 occurs in the V_2 veins and commonly occurs with Tbi2 (Fig. 9B). These grains are < 0.5 mm and, like Au1, have varying shapes with irregular edges with associated Ag (3.55 wt%,) Hg (3.13%), and Bi (0.96 wt%). Au2 also occurs as an inclusion in Py4a (Fig. 9C). Au3 (remobilized) was observed in microfractures in the subarkosic unit and V_2 veins and microfractures within Apy and Py4a (Fig. 9D–F). In the case of Figure 9D, the gold, Au3, is associated with fractures crosscutting the V_2 vein and thus has a later timing. The gold grains associated with remobilization, Au3, are associated with Ag (4.4 wt%), Hg 3.12 (wt%), and Bi (0.7 wt%; Supplementary Data File A).

4.3 Summary of LA-ICP-MS Element Maps

A total of 19 LA-ICP-MS semi-quantitative element maps from 13 thin sections were collected on pyrite, pyrrhotite, chalcopyrite, arsenopyrite, and sphalerite, with various host lithologies including calc-silicate alteration within mafic volcanic rocks, smoky quartz veins, pegmatite, and the subarkose unit of the Porky Lake Group. The principal elements of interest in this study include Fe, Co, Ni, Cu, As, Se, Mo, Ag, Sb, Te, Au Pb, Tl, and Bi; these elements were selected because several of them, such as As-Ag-Sb-Te-Bi (e.g., Helmy et al., 2010; Vikent'eva and Vikentev, 2016), can substitute into a sulfide mineral lattice and are enriched in orogenic gold deposits (e.g., Sibson et al., 1988; Groves et al., 1998, 2018; Cox, 1999). The total list of elements analyzed is found in Supplementary Data File B. Furthermore, these elements were best represented across the sulfide mineral phases, whereas elements such as W that can be associated with magmatic-hydrothermal deposits (e.g., Ispolatov et al., 2008; Mathieu, 2019; Beaudin et al., in revision) were not present at high concentrations in the Porky deposits. The selected maps focus on the pyrite and arsenopyrite generations associated with the calc-silicate alteration (Fig. 10A), V_2 veins and remobilization (Fig. 10B, 11A-11B, 12A), and metamorphism (Fig. 12B); additional sulfide mineral maps are provided as Supplementary Data File D as Figures S1–8.

4.3.1 Observed Sulfide Minerals and Corresponding Elemental Associations

Given their small size and trace occurrence, the sulfide minerals of the V_1 veins were not analyzed by LA-ICP-MS; however, through microprobe analyses, Po1 shows the highest Co-Mo concentration (averages of 2,300 and 300 ppm, respectively) of all sulfide generations (Table 1). Py2, a colloform pyrite observed in the subarkose arenite unit (Fig. 7B, 10A), is inferred to be the oldest sulfide generation in the Porky Lake Group due to the dissolution textures and being overprinted by the Py4a generation. It exhibits observed elevated concentrations of Ni-As-Ag-Pb-Tl (5,074, 20,562, 564, 17,832, and 169 ppm, respectively) compared to all subsequent sulfide generations, along with the second highest Cu content (1,501 ppm; surpassed only by Py4b), the second highest Mo content (14 ppm; exceeded only by Po1), and the second highest Bi concentration (27 ppm; behind Py4a). As such, this sulfide generation represents a significant increase in base metals in the system prior to the main mineralization stages (Fig. 13, S1; Table 1). Within the calc-silicate alteration, Po2/Py3 occurs in the mafic volcanic unit with Au1 occurring along grain boundaries between Ccp2-Sp (Fig. 10A). Despite occurring in the mafic volcanic rock, these sulfide minerals lack significant base metal concentration when compared to the other phases (Fig. 13, S2; Table 1). In the Py4a grains, Au2 occurs in areas with increased Ni-As-Se with Py2 (Fig. 10B). Relative to all sulfide generations, Py4a shows the highest Au-Bi concentrations (2 and 55 ppm, respectively), and Au-rich inclusions are associated with Ag-Te-Pb-Bi (Fig. 13, S3). Euhedral Py4a grains associated with V_2 veins in the subarkose arenite unit often exhibit a core with Co that grades to an enriched Ni-Se-Sb rim within a given grain (Fig. 11A). Despite elevated Co in the Py4a core, this sulfide generation largely lacks Co but is enriched in Ni-As-Pb second only to Py2 (4,157, 13,151, and 11,465 ppm, respectively) and contains the highest concentrations of Bi with 55 ppm (Fig. S1; Table 1). Py4b is associated with Py4a and occurs as disseminated anhedral grains, commonly forming with Ccp3 (Fig. 11A). This generation shows the highest Cu concentration (31,939 ppm) and is attributed to forming a disseminated matrix with Ccp3. When comparing elements between Py4a/b, the Py4b shows a decrease in the concentration of the rest of the elements. Apy grains, which also occur in the smoky quartz veins (V_2) and are associated with Au2, are characterized by dissolution features and anhedral morphology with the highest concentration of Sb-Te of all sulfide generations (130 and 26 ppm, respectively; Fig. 11B, S4–5). Inclusion-rich Apy, with Po, Py, and Ccp inclusions (Fig. 12A), exhibit increased Co-Ni-As-Se-Sb concentration, with Po inclusions containing the highest Au2 concentration and associated Ni-Mo-Ag-Pb-Tl-Bi. Increased Co-Ni-Cu content often occurs as zonation in all Apy grains. Subsequent microprobe analyses revealed trace stibarsen associated with gold mineralization and further support that As-Sb correlate with mineralization. Similarly, the Apy grains have elevated Sb when compared to the Po/Py grains (Table 1). The Po4/Py5/Ilm2 grains, which tend to be small and anhedral, are aligned with foliation. These grains display microfractures, revealed by LA-ICP-MS, with associated Pb-Tl-Bi (Fig. 12B, S6). Py6a represents remobilized pyrite that formed around brecciated quartz, biotite, and muscovite grains (Fig. 7G, S7). Lastly, Py6b involves crystal lattice controlled exsolution with subparallel horizontal bands; Py6b occurs in Py4a and displays lower trace element concentrations compared to the host sulfide mineral with the exception of Pb (11,478 ppm), which occurs at a similar concentration as in Py4a (11,465 ppm; Fig. 7H, 13, S8).

4.4 Geochronology

The samples form a linear array on a Concordia diagram (Fig 14A; Table 2; Supplementary Data File C). A geological date can be determined by using either the weighted average or the age of the upper intercept with the Concordia curve. This allows for filtering the data based on criteria such as inheritance, Pb-loss, or metamorphic overprint (e.g., Condon et al., 2024). Analysis z10, which is significantly older and has an anomalously high amount of non-radiogenic Pb, is excluded in all calculations. A weighted mean age of 1843.7 ± 1.4 Ma, with $^{206}Pb/^{238}U$ and $^{207}Pb/^{235}U$, (2σ, MSWD=6.3, p<<1; S10) results from 13 zircon analyses that form a distinct cluster population and excludes z10 and the three youngest grains. An upper intercept age of 1841.8 ± 4.5 Ma (2σ, MSWD=0.38, p=0.54; Fig 14A) results when excluding z10 and the three youngest grains that are close to the age of metamorphism. The cross-cutting, intrusive relationship of the ca. 1842 Ma granodiorite with Porky Lake Group is shown in Fig. 14.

4.5 Constraints on Physiochemical Conditions

The physiochemical conditions of mineralization provide crucial insights into the evolution of hydrothermal fluids and their relationship with deformation. In this section, we integrate mineral thermobarometry and sulfide mineral chemistry to refine the temperature, pressure, and fluid composition during gold deposition of the Porky Main and Porky West deposits.

To determine the potential temperature and pressure conditions of the V_2 veins, Chl and Bt2 were used due to their association with proximal gold and sulfide mineralization within the V_2

veins. Using the chlorite analyses, the Fe/(Fe + Mg) molar ratios were calculated. Three geothermometer calculations were selected: Cathelineau (1988; T = 321 * Al_{IV} – 69); Kranidiotis & MacLean (1987; T = 106 * Al_{IV} correlation + 18); and Zang & Fyfe (1995; T = 106.2 * Al_{IV} correlation + 17.5). These were selected to compare with previous results obtained from rock samples from the Seabee Gold Operation (i.e., Beaudin et al., 2024) and are represented in Supplementary Fig. S9A–D and Supplementary Data File A. Geothermometery calculations from n = 4 chlorite analyses, plotted on a ternary (Al + Q)-Mg-Fe classification diagram after Zane & Weiss (1998 (Fig. S9A), yielded corresponding temperatures of ~315ºC, and 303ºC, using the Kranidiotis & MacLean (1987) and Cathelineau (1988) methods, respectively. These temperatures could represent retrograde metamorphism as the biotite in V_2 veins often had irregular grain boundaries with chlorite forming around the grains. These temperatures are higher than Zang & Fyfe (1995) (average 218ºC). This could be attributed to the Chl with high XFe values, where Fe substitutes into octahedral sites and reduces Al(iv) and leads to lower apparent temperatures with the Zang & Fyfe (1995) method, whereas Kranidiotis & MacLean (1987 partially correct for Fe-Mg substitution. These ranges fall in the 300 ± 50ºC formation with orogenic gold deposits (Goldfarb and Groves, 2015). In contrast, diopside and K-feldspar occur with the calc-silicate alteration that is inferred to have occurred before the V_2 veins; given this mineral composition, this suggests higher temperature fluids of ~525ºC (McCuaig and Kerrich, 1998).

The pressure conditions of mineralization were estimated using Bt2 grains as they have an association with the smoky quartz veins and are spatially associated with visible gold and arsenopyrite grains in various lithologies. Using biotite grains (n = 8) plotted in an Mg–(Fe^{2+} + Mn)–(Al^6 + Fe^{3+} + Ti) diagram after Foster (1960) and empirical calculations using Uchida et al. (2007; Fig. S9B and Supplementary Data File A), the gold/sulfide mineralization yielded values consistent with formation at ~3.1 kbar or ~10.2 km depth (Willson, 2010). These values are consistent with the proposed range of 4–15 km depth for orogenic gold deposits forming at the transitional-ductile brittle boundary (Groves et al., 2020). Amphibole compositions were also plotted on Ca-Mg-Fe-Mn-Li and calcic amphibole classification diagrams after Leake et al. (1997), and although these were not used for empirical calculations, they show a consistent amphibole trend between the Porky, Santoy, and Fisher areas with chlorite and biotite being Fe-abundant and favoring the formation of Mg-rich hornblende, actinolite, and minor Fe-pargasite and edenite (Fig. S9C–D).

Co/Ni ratios have been used to identify fluid sources in sulfide minerals (e.g., Gao et al., 2019; Mathieu, 2019; Cardenas-Vera et al., 2023). Metamorphic fluids typically have a ratio close to 1 (Mao et al., 2009; Chen et al., 2015), whereas sedimentary sulfide minerals often exhibit a weighted Co/Ni average ratio of 0.32. Hydrothermal sulfide minerals show Co concentrations of ~1 to 60 ppm and Ni concentrations of ~40 to 1,000 ppm, resulting in a Co/Ni ratio of 1.09. Volcanogenic sulfide minerals exhibit Co concentrations ranging from ~80 to 5,000 ppm and Ni concentrations of ~10 to 700 ppm, corresponding to a ratio of 7.15. Magmatic sulfide minerals have Co concentrations of ~1,025 to 10,100 ppm and Ni concentrations of ~800 to 7,000 ppm, with a ratio of 1.45 (Zhang et al., 2016). Using LA-ICP-MS data (Supplementary Data File B), pyrite has low Co/Ni ratios. Py2 in the subarkosic unit has average Co and Ni concentrations of 1 ppm and 5,074 ppm, respectively, and the Py4a in the V_2 veins has average Co and Ni concentrations of 1 ppm and 4,157 ppm, respectively. The Co/Ni ratios recorded by Po and Apy are higher. The Po2 in the calc-silicate alteration contains average Co and Ni concentrations of 14 ppm and 254 ppm, respectively, with a ratio of 0.055. The Apy within these veins has average Co and Ni concentrations of 370 ppm and 645 ppm, respectively, giving a ratio of 0.57. Lastly, the

Po4, presumed to be associated with metamorphism, has average Co and Ni concentrations of 503 ppm and 2,015 ppm, respectively, with a ratio of 0.25.

5 Discussion

Orogenic gold formation is typically attributed to metamorphic fluids (e.g., Groves et al., 1998, 2018; Goldfarb et al., 2001, Goldfarb and Groves, 2015, Patten et al., 2020); yet, more detailed geochronological studies suggest that these deposits are multi-stage and may be related to both igneous and metamorphic events (Morelli et al., 2005; Cook et al., 2013; Lawley et al., 2015, 2020; Rubingh et al., 2024). Furthermore, these orogenic deposits commonly share a spatial and temporal relationship with sedimentary basins that form during orogenesis, such as those related to Timiskaming-type basins in the Abitibi greenstone belt (Poulsen et al., 1992).

To aid in the understanding of gold mineralization of the Porky deposits, a paragenetic sequence was developed (Fig. 8) and the geochemical composition of sulfide minerals, including those associated with gold, was analyzed. Known mineralization in the Porky Lake system (as represented by the Porky Main and Porky West deposits) occurs along a ~12 km long, openly-folded shear zone along the contact separating the Porky Lake Group from the mafic volcanic units of Assemblage A (Fig. 2). Detailed petrographic and LA-ICP-MS analyses show that visible gold, gold inclusions, and Au bound in sulfide mineral lattices occur in all rock units associated with the contact shear zone; thus, host rocks of the Porky Lake system include mafic volcanic rocks of Assemblage A, arenite and conglomerate of the Porky Lake Group, and various intrusive units. In the mafic volcanic rocks, visible gold (Au1) is hosted in calc-silicate alteration of the mafic volcanic unit at both Porky Main and Porky West. Visible gold (Au2) is also hosted in smoky quartz veins; these veins are most abundant at Porky West and commonly found in the Porky Lake Group but are also found in all units. The distribution of gold within both calc-silicate alteration and smoky quartz veins suggests fluctuating fluid compositions, as evidenced by the oscillatory zonation in Apy and Py4a. Together with gold observed in the calc-silicate alteration, as inclusions in Apy (Fig. 11B) and as late, fracture-filling within various sulfide minerals, including the more disseminated Apy grains, the Porky deposits likely underwent two primary stages of Au formation (Au1, Au2), followed by a third event during which Au in the sulfide minerals was liberated and remobilized in brittle fractures to form Au3.

Gold transport and deposition are commonly attributed to hydrothermal fluids; however, recent studies indicate that polymetallic melts may also serve as an important transport medium for gold during metamorphism, particularly in the presence of chalcophile elements such as Sb, Bi, Te, and Hg (Hastie et al., 2020; Tait et al., 2023). These elements significantly lower the melting temperature of gold, allowing remobilization at much lower temperatures than previously thought. For instance, Bi can lower the melting temperature of gold from 1,064°C to <300°C (Tomkins et al., 2004). Microprobe analyses of gold grains from the Porky deposits revealed elevated Bi (up to 0.96 wt%) and Hg (up to 3.13 wt%), suggesting that these elements played a role in stabilizing gold in a low-temperature melt phase. Furthermore, remobilized gold, Au3, was observed in microfractures within various sulfide minerals, with one instance in Po2-Ccp2-Sp with associated Sb (up to 2,325 ppm), Te (up to 33 ppm), and Bi (up to 13,311 ppm; Fig. 10A). In addition, Figure 13 shows that the sulfide minerals associated with gold mineralization (i.e., Po2, Py4a, and Py4b) exhibit Au concentrations between ~0.008 and 2 ppm, indicating that the sulfide minerals themselves are not a significant source of Au mineralization. The porous textures of the Apy also indicate dissolution-reprecipitation reactions that operate at the scale of individual grains, during which pre-existing gold, either present as submicroscopic inclusions or structurally bound within the sulfide lattice may be liberated and subsequently reprecipitated within newly formed pore space. These textures are similar to the Apy gold-bearing grains of the Lynn Lake deposits (Hastie et al., 2018). This suggests that gold is more likely associated with redistribution processes such as Ostwald ripening and dissolution-reprecipitation rather than primary incorporation of gold during sulfide growth, and that gold in the Porky deposits was not solely transported by hydrothermal fluids but potentially also by polymetallic melts, fundamentally altering our understanding of the mineralizing system. Furthermore, the Apy grains have a 0.57 Co/Ni ratio closer to the magmatic-metamorphic fluid range of 1.17-5 (Hou et al., 2016). Magmatic deposits favor a polymetallic Au (Sillitoe and Thompson, 1998); tellurobismuthite was associated with Au1 and Au2 and various sulfide minerals, such as arsenopyrite, in the Porky deposits. Likewise, sphalerite and trace galena were observed in the calc-silicate alteration and as inclusions in the arsenopyrite, suggesting that magmatic-hydrothermal fluid may have introduced early low-grade gold into the system that was subsequently upgraded and/or that these magmatic-hydrothermal fluids were present during on-going and evolving orogenesis. However, at low fluid-to-rock ratios, fluid composition may be strongly modified by interaction with surrounding lithologies and therefore may not uniquely reflect their source as is the case for the Porky Lake area, where the abundant volcanic rocks and intrusions may import a magmatic-like geochemical signature to fluids that were otherwise predominantly metamorphic in origin. Lastly, zircon and monazite grains were observed as inclusions in Apy; we speculate these inclusions potentially formed during peak metamorphism and were pre- or coeval to the formation of the host Apy. These Apy grains further show monazite overgrowth on the rims, which we further speculate is attributed to fluid-assisted recrystallization during retrograde (Schneider et al., 2007) as rocks of the Glennie domain underwent rapid uplift and cooling.

Overall, the results presented in this study suggest that gold mineralization of the Porky Main and Porky West deposits involved complex fluid interactions, polymetallic melt contributions, and multi-stage mineralizing events. Geochemical data, including Bi-Hg enrichment in gold, Co/Ni ratios in sulfide minerals, and LA-ICP-MS element maps, provide strong evidence that polymetallic melts contributed to gold remobilization alongside hydrothermal activity associated with early igneous and later metamorphic processes. However, without absolute ages on the zircon and monazite inclusions of the arsenopyrite grains, the timing of these events is conjectural.

5.1 Significance of Geochronological Constraints of the Porky Lake Group

Initially, it was thought that the Porky Lake Group was younger than the ca. 1838 Ma Assemblage B (Delaney and Cutler, 1992; McNicoll et al., 1992), with a minimum age only constrained by peak metamorphism 1810 ± 10 Ma (Schneider et al., 2007). Furthermore, primary depositional features of the unconformity surface, if it existed, have been structurally overprinted; however, mafic volcanic clasts occur within the conglomerate units, consistent with erosion of the ca. 1.88 to 1.87 Ga Assemblage A. By contrast, an unconformity surface is preserved between Assemblages A and B (Delaney, 1986; Durocher et al., 1992). The new age for the granodiorite, 1841.8 ± 4.5 Ma provides a minimum age for the Porky Lake Group. Deposition of the Porky Lake Group must have occurred sometime after Assemblage A volcanism ended (post ca. 1879 ± 1.3 Ma (Witvoet, 2023)). In addition, the ca. 1859 Ma Eyaphaise pluton that intrudes Assemblage A further provides a minimum age constraint. The age of ca. 1842 Ma implies that the deposition of the Porky Lake Group must have occurred between the two major volcanic assemblages of the Pine Lake greenstone belt and is a significant change to the inferred stratigraphy (cf. Delaney, 2016). The new granodiorite age presented here suggests that the Porky Lake Group was likely buried by the time Assemblage B deposition commenced ca. 1838 Ma. In this scenario, the granodiorite could represent the subsurface intrusive equivalent of Assemblage B felsic intrusive rocks. Nevertheless, the precision of the new age for the granodiorite precludes a confident assignment of an older age for the Porky Lake Group. Furthermore, the extrusive volcanic rocks that are associated with Assemblage B are completely absent in the Porky Lake Group, suggesting that they formed at different times and in different environments, rather than being coeval.

5.2 Metallogenic Stages of the Porky Gold Mineralization

The six stages that led to the development of gold mineralization in the Porky Lake system are shown in Figure 15, which illustrates the relationships between the host rocks, structures, alteration, and mineralization.

Stage one includes the formation of calc-silicate veins (V_1) in the Assemblage A units (Fig. 15A). These veins formed prior to the deposition of the Porky Lake Group because they are absent in the sedimentary and intrusive units. Although, these veins do not show visible gold, have only trace sulfide minerals, and do not show any cross-cutting relationships with subsequent veining, their calc-silicate mineralogy is consistent with the calc-silicate alteration that is associated with the early Au1 event suggesting they may be coeval. Within these veins, the associated Po1-Py1-Ccp1 show the highest concentration of Co-Mo of any sulfide generation (Fig. 10A).

Stage two: This stage encompasses both the deposition of the host rocks as well as an early introduction of gold into the system throughout D_2. We interpret that the Porky Lake Group was unconformably deposited on the Assemblage A mafic volcanic rocks, potentially during the uplift of Assemblage A rocks (Fig. 15B). The granodiorite and quartz diorite were emplaced during this stage. Given the polymetallic signature of the deposit and the presence of tellurobismuthite associated with gold mineralization, these intrusive units may have incorporated early low-grade gold into the Porky Lake system, but are not definitive evidence that magmatic-hydrothermal fluids were involved After the intrusion of the granodiorite unit, D_2 shear zones formed on and near the contact of the Porky Lake Group with Assemblage A. The early colloform Py2 formed during this stage, but without obvious S_2 and Py2 relationships, it may have formed prior to D_2, which accounts for its trace occurrence and subsequent overprinting by Py4a. At this time, sulfide mineralization (Py2) contained elevated Ni-As-Ag-Sb-Pb-Tl- when compared with all subsequent sulfide generations and the second highest Cu-Mo-Bi concentrations with respect to Po1, Py4a, and Py4b.

Stage three includes the development of the pervasive calc-silicate alteration along the sheared contact (Fig. 15C) and the deposition of visible gold (Au1) with Po2-Ccp2-Py3-Sp-Gn. During this phase, visible gold developed in the mafic volcanic unit. Furthermore, similar mineral paragenesis between the Porky Main and Porky West deposits, the Santoy Mine Complex, and the Fisher property support an interconnected system with pervasive and foliation-parallel calc-silicate alteration consisting of Di-Ser-Pl-Bt-Ms-Kfs-Cal-Aug-Ttn-Ap ± Chl that occurs in the volcanic units (Beaudin et al., 2024; Table 3). In addition, the calc-silicate alteration was observed as boudins in outcrop and underground at Santoy (Wood, 2016), which further confirms that this alteration occurred before D_3 deformation i.e., D_2. Together, these observations suggest that the calc-silicate alteration represents an early, system-wide alteration framework with its present mineralogy reflecting metamorphic re-equilibration of an originally carbonate- and silicate-rich hydrothermal assemblage.

Stage four encompasses the formation of the V_2 veins. This stage is regarded as the main gold source due to the frequent nature of visible gold (Au2) observed in drill core. We consider that the V_2 veins with their visible gold and Apy-Py4a/b-Po3-Ccp3 association formed after the fluid pulses responsible for the V_1 generation of veins and the calc-silicate alteration (Fig. 15D). This fluid phase **r**esulted in sulfide mineral deposition with elevated Co-Ni-As-Se-Mo-Ag-Sb-Te-Tl-Bi, with the highest observed Bi concentration of all sulfide mineral generations and the second highest Ni-As-Pb concentration (after Py2), whereas the Apy grains show the highest Sb-Te of all sulfide generations. Oscillatory zonation throughout the Apy grains and in Py4a suggests that gold was incorporated into the crystal lattice between parts of the mineral grain that had different Co and Ni-Se. In addition, the Py4a/b-Po3-Ccp3 sulfide minerals associated with the V_2 veins have Co/Ni ratios that are consistent with hydrothermal fluids with a depleted Co input, whereas the Apy grains have a ratio closer to that of magmatic-metamorphic fluids, suggesting that they may have formed from a pulse of later fluid pulse: this might account for the Py4a-Po3-Ccp3 and Apy rarely being observed together, but rather in separate V_2 veins. In addition, empirical calculations of chlorite and biotite associated with this vein generation were used for pressure and temperature conditions. Empirical chlorite and biotite thermobarometry calculations suggest that these veins formed at 315ºC and 3.1 kbar or 10.2 km depth. In comparison to the Fisher property and Santoy mine area (Fig. 2), Beaudin et al. (2024) performed similar empirical calculations on biotite and chlorite and obtained the following temperature and pressure conditions: Fisher: ~310–320ºC, 3 kbar; Santoy: ~360ºC, 2–3 kbar (Fig. S9A–B). Furthermore, Tourigny et al. (2004) conducted fluid inclusion studies on samples from the Seabee mine (Fig. 2), identifying conditions of ~370ºC and 1.1–2.5 kbar. The values obtained for the Porky deposits are comparable between Fisher, Santoy, and Seabee and further support the suggestion that they form part of an interconnected orogenic gold system. The V_2 veins also show transposition, folding, and boudinage, which may have resulted from ongoing D_2 deformation. At Santoy, boudinaged quartz veins occur along the western limb of the Carruthers Lake synform and are similar to those of the Ray Lake synform, suggesting similar flattening and transposition along the fold limbs during D_3 deformation/shearing (Wood, 2016).

Stage five: The Porky Lake deposits were subjected to peak metamorphism at ca. 1810 Ma during late D_2, which attained temperatures and pressures of ~500–650ºC and 2.5–7 kbar (Durocher, 1997). During this time, Po4/Py5 were transposed into foliation (Fig. 12B, 15E).

Stage six represents the remobilization of gold that dramatically impacted its present distribution. This gold was remobilized from Po2-Ccp2-Py3, Py4a/b-Ccp3, and Apy during the transition to brittle deformation with the formation of Py6a/b in fractures as the rocks were slowly being exhumed (Fig. 15F). Previous age determinations for gold mineralization within the Seabee Gold Operation include clustering of ca. 1.77 to 1.76 Ga ages (Schultz, 1996; Wood, 2016; Beaudin et al., in revision), all of which considerably postdate the host rocks in their respective areas. The proposed timing of gold mineralization in the Porky deposits is significantly earlier than existing gold mineralization in the Seabee Gold Operation. We interpret that the ca. 1.77 to 1.76 Ga ages most likely represent remobilization and not the primary orogenic gold mineralization event; however, new fluid pulses could have introduced a new phase of gold into the Seabee Gold Operation area at this time.

5.3 Comparisons of Similar Orogenic Gold Deposits in the Trans-Hudson Orogen

Paleoproterozoic deposits from the Snow Lake camp in Manitoba (Rubingh et al., 2024) and the Meliadine Gold District in Nunavut (Lawley et al., 2015) are both defined by multistage orogenic gold occurrences that formed before peak metamorphism. Comparison with these deposits, including the composition of arsenopyrite at Porky Lake, can be useful to determine whether these deposits share similar stages in their orogenic gold mineralization.

Snow Lake: Mineralization at the New Britannia deposit occurred before peak metamorphism in the Trans-Hudson orogen, with gold found as micro-inclusions aligned with foliation, followed by remobilization during progressive thrusting and folding (Rubingh et al., 2024). Gold in the Porky Main and Porky West deposits is found in V_2 veins and a calc-silicate alteration that is semi-concordant to concordant to foliation, transposed, boudinaged, and folded, indicating deposition pre-peak metamorphism (Fig. 4D). The Snow Lake arsenopyrite grains exhibit elevated Co-Ni-Pb-Bi on their rims, whereas the Porky grains show oscillatory zonation of Co-Ni-Te throughout the mineral grain (Fig. 12A).

Meliadine Gold District: Mineralization at Meliadine is hosted in quartz veins that are folded, boudinaged, and transposed parallel to the main deposit fabric, suggesting that veining and sulfide minerals predate or are synchronous with the primary deposit fabric (Lawley et al., 2015); these features are similar to the V_2 smoky quartz veins of the Porky Main and Porky West deposits (Fig. 4D). Several arsenopyrite grains at Meliadine preserve local oscillatory zoning with cores relatively enriched in Ni-Se-Mo-Sb-Te (Lawley et al., 2015); arsenopyrite grains in the Porky Main and Porky West deposits show similar oscillatory zonation with Fe-Co-Ni-As-Se-Mo-Sb-Te (Fig. 10B). Arsenopyrite grains in both areas often have coarse-grained gold occurring in adjacent quartz veins, interpreted to represent gold remobilization enrichment after the post-crystallization history of earlier sulfide minerals. Sieve-textured arsenopyrite grains typical of metamorphosed deposits (Tomkins and Mavrogenes, 2001) are also observed in both areas, further confirming that initial mineralization occurred during D_2. Lastly, fractured Au-rich arsenopyrite grains with associated Co-Ni-Zn-Pb-Bi were observed at Meliadine (Lawley et al., 2015); in contrast, the remobilized gold in fractures at Porky shows increased Ag-Pb-Tl-Bi (Fig. 10A).

Overall, the results presented in this study suggest that gold mineralization of the Porky Main and Porky West deposits involved complex and changing hydrothermal fluids, evolving geodynamic conditions, and multi-stage mineralization similar to the Paleoproterozoic Snow Lake camp and Meliadine Gold District; this suggests the potential for earlier stages of mineralization elsewhere in the Trans-Hudson orogen.

6 Conclusion

Defining the timing, fluid evolution, and sources of gold mineralization in orogenic gold deposits is important for understanding these systems and choosing effective exploration targets. This study characterizes the mineral associations of the gold in the host rocks of the Porky Lake system for the first time, providing a better understanding of its mineralization history in the context of other orogenic gold deposits hosted in the Pine Lake greenstone belt. New geochronological data of a granodiorite intruding the Porky Lake Group indicate an age of ca. 1842 Ma, establishing a minimum depositional age for the Porky Lake Group. While its new age constraint suggests that it likely pre-dates the ca. 1838 Ma rhyolite that marks the base of Assemblage B, the error does not preclude that it could be coeval with Assemblage B. However, this scenario does not account for the different rock types between the volcanic rock-dominated Assemblage B and the siliciclastic Porky Lake Group, and the time required to bury the Porky Lake Group to a depth at which it would be intruded.

Early gold introduction is attributed to magmatic-hydrothermal fluids that were subsequently upgraded during ongoing orogenesis. The primary host of gold mineralization within the Porky deposits is the V_2 vein set, which shows evidence of transposition, folding, and boudinage, suggesting these veins likely formed during early D_2. Several phases of gold-associated sulfide minerals were identified within a paragenetic sequence, including Po2-Py3-Ccp2-Sp-Gn in the calc-silicate alteration of mafic volcanic units and Apy-Py4a/b-Ccp3-Po3 in the V_2 veins. Evidence of gold remobilization in fractures within earlier Apy-Py4a minerals and across quartz grain boundaries suggests this occurred during the transition to brittle deformation. Gold mineralization is thought to have formed ca. 1780 to 1745 Ma during D_3 throughout the Seabee Gold Operation, based on the geochronology of mineral associations with gold (Schultz, 1996; Wood, 2016; Beaudin et al., in revision). However, the data from this study indicate that initial gold mineralization at Porky Lake predates D_3, suggesting that younger ages elsewhere in the Seabee Gold Operation may represent later remobilization of gold, as seen in the Porky deposits. This interpretation is further supported by similar gold-sulfide mineral associations, vein generations, and calc-silicate alteration in other Seabee Gold Operation deposits, such as those at Santoy and Fisher. The observed similarities across the Pine Lake greenstone belt are consistent with a regional orogenic gold system during the Trans-Hudson orogen.

Data Availability

The data for the study are available within the Supplementary Data Files.

Acknowledgments

The research was supported by a Natural Sciences and Engineering Research Council of Canada (NSERC) Alliance grant (ALLRP 555177 - 20) to K.A. and C.A.P. in collaboration with SSR Mining, as well as an NSERC Canada Graduate Scholarship - Masters and a Society of Economic Geologists Student Fellowship to D.D. This paper forms part of an M.Sc. thesis at the University of Saskatchewan by D.D. Staff at SSR Mining are thanked for their logistical assistance on-site and geology discussions. P. Yang is thanked for assistance in the electron microprobe laboratory at the University of Manitoba.

Declaration of Competing Interest

Competing interests: The authors declare there are no competing interests.

Figure Captions:

Figure 1. Trans-Hudson orogen subdivisions of northern Saskatchewan and Manitoba. The red star indicates the Seabee Gold Operation. Map modified after Corrigan et al. (2007) with updated domain boundaries with the most recent map data sourced from the Saskatchewan GeoAtlas (2023) and Manitoba Geology Map Gallery (2023) using NAD83 with a Mercator map projection with latitude-longitude coordinates. The yellow star indicates the New Britannia Mine in the Flin Flon Domain and was included as this study compares gold mineralization in that area. Meliadine Gold District is also referenced but is outside the map constraints and is north of Rankin Inlet, Nunavut. Major regional structures include RLSZ = Reilly Lake shear zone, DLSZ = Duck Lake shear zone, MLTZ = McLennan Lake tectonic zone, NFSZ = Needle Falls shear zone, PLSZ = Parker Lake shear zone, SFZ = Stanley fault zone, ORSZ = Owl River shear zone, GLSZ = Granville Lake structural zone, and SBZ = Superior boundary zone.

Figure 2. Simplified 1:250,000 geological map of the Pine Lake greenstone belt and area surrounding the Seabee Gold Operation, northern Saskatchewan, UTM NAD83 Zone 13N, Mercator map projection, with the most recent map data sourced from the Saskatchewan GeoATLAS Mapping (2023); gold occurrences (yellow star) from SRK Consulting (2017). Water bodies have been omitted for clarity. The study area is indicated by the black box near the Porky deposits.

Figure 3. A. Geological map of the Porky West and Porky Main deposits along a mineralized shear zone. PLG = Porky Lake Group, ASA = Assemblage A, ASB = Assemblage B, PW = Porky West, PM = Porky Main. Map data based on Saskatchewan GeoATLAS Mapping (2023). **B.** The schematic cross-section is based on a drillhole plunging from X-Y. **C.** Simplified stratigraphy of the area showing the relationship with the Porky Lake Group and Assemblage B with Assemblage A.

Figure 4. Rock units present at the Porky Main and Porky West deposits. **A.** Mafic volcanic rock along a mineralized shear zone with V_1 veins. **B.** Folded V_1 veins in an intermediate rock. **C.** Conglomerates in the subarkosic unit that has clasts aligned to foliation. **D.** Rotated and boudinaged V_2 veins with subsequent folding in the subarkosic unit. **E.** Granodiorite (left) and mafic volcanic (right) contact. **F.** Pegmatite (bottom) cutting the subarkosic unit (top).

Figure 5. Calc-silicate alteration, veins, and host lithologies in drillcore. The alteration and veins commonly have irregular margins and are semi-concordant and concordant to foliation. **A.** Calc-silicate V_1 veins in a mafic volcanic rock. **B.** Pervasive calc-silicate alteration in an altered mafic volcanic rock. **C.** V_2 veins with arsenopyrite (Apy) and visible gold are focused along the vein margins in the subarkosic unit.

Figure 6. Photomicrographs of rock units (unmineralized) from the study area. Field of view (FOV) = 4.5 mm. **A.** Plane polarized light (PPL) of mafic volcanic unit with S_1/S_2 foliation. **B.** PPL of intermediate volcanic unit with S_2 foliation defined primarily by Hbl-Bt-Qz. **C.** PPL of conglomerate in the subarkosic unit. **D.** Cross-polarized light (XPL) of subarkosic unit; S_1/S_2

foliation defined by Ms and Qz. **E.** PPL of wacke with S_2 foliation defined by fibrolite and Bt. **F.** PPL of same wacke showing garnet with Po4 forming around the rim. **G.** PPL of porphyritic granodiorite with Py5 grains; S_2 foliation defined by Pl-Ms-Qz. This unit was used for geochronology to constrain the age of the Porky Lake Group. **H.** PPL of quartz diorite; S_1/S_2 foliation defined by alignment of Bt. **I.** PPL of early K-feldspar pegmatite with Grt. **J.** PPL of calc-silicate V1 vein on the margin of the mafic volcanic unit. **K.** Pervasive calc-silicate alteration with Ser-Di2-Pl2-Qz2. **L.** XPL in V2 vein showing grain boundaries with visible Tbi2/Au2 grains.

Figure 7. Photomicrographs of representative sulfide mineral generations (reflected light); yellow boxes indicate areas used for LA-ICP-MS. The sulfide mineral shapes were used to represent the sulfide generations in Fig. 14. **A.** Trace pyrrhotite-pyrite-chalcopyrite (Po1-Py1-Ccp1) of the V_1 veins. **B.** Early colloform Py2 occurs as a trace sulfide in the subarkosic unit with Py4a when associated with V_2 veins. **C.** Porous Po2-Ccp2-Sp of the pervasive calc-silicate alteration in the mafic volcanic unit; also associated with Py3-Gn. **D.** Euhedral Py4a and disseminated Ccp3-Py4b associated with V_2 veins. **E.** Anhedral Apy with dissolution and gold forming in microfractures. **F.** Inclusion-rich Apy in the pegmatite unit. Metamorphic-associated Po4 (Fig. 6F–G) is associated with Py5 in the intrusive units. **G.** Remobilized Py6a occurs around brecciated Qt-Ms-Bt grains. **H.** Py6b with crystal lattice controlled exsolution and subparallel horizontal bands from an earlier Py4a. The Py6b has been traced for clarity.

Figure 8. Mineral paragenesis for the Porky Main and Porky West deposits by geological unit. Three generations of gold occur: Au1 in the calc-silicate alteration of the mafic volcanic rock, Au2 in smoky quartz veins, and Au3 as remobilized gold in all units.

Figure 9. Backscattered electron images of the three gold phases. **A.** Visible Au1 in calc-silicate alteration of the mafic volcanic rocks and associated Ttn-Ms1-Di2-Pl2-Qz2. **B.** Visible Au2 with Tbi2 in V_2 vein. **C.** Au2 inclusion in Py4a. **D**. V_2 vein (top) and subarkosic unit (bottom) with Au3 forming in a fracture cutting both units. **E.** Remobilization of Au3 in Apy fractures with dissolution; ilmenite inclusions in Apy. **F.** Remobilization of Au3 in brecciated Py4a.

Figure 10. LA-ICP-MS semi-quantitative element maps. In Figures 10, 11, and 12, the yellow box correlates to the analyzed area. **A.** Po2/Ccp2/Sp and associated calc-silicate alteration with calcite as inclusions and matrix surrounding the grains where the Po2 is traced in red. Au has been liberated from the sulfide minerals and is now host in microfractures with corresponding Ag-Sb-Pb-Tl-Bi along the Po2-Ccp2 boundary. All concentrations are in ppm and elements with an * indicate maps displayed to the 99th percentile to reduce inclusions. In doing so, inclusions appear larger, but element concentration is better observed throughout the remaining sulfide mineral. When ignoring the 99th percentile, the maximum values of these include Ag* = 612 ppm, Sb* = 2,325 ppm, Te* = 33 ppm, Au* = 6 ppm, Pb* = 5,262 ppm, Tl* = 10 ppm, and Bi* = 13,311 ppm. **B.** Colloform Py2, traced in blue, in a V_2 vein adjacent to Py4a, traced in red, in the subarkosic unit. This early pyrite generation is enriched in Ni-Cu-As-Se-Mo-Ag-Sb-Pb-Tl-Bi when compared to the Py4a, whereas Au is found in the crystal lattice in the Py4a with a Ni-As-Se association, where Co* = 75 ppm.

Figure 11. LA-ICP-MS semi-quantitative element maps. **A.** Euhedral Py4a, traced in red, and disseminated Py4b/Ccp3, with Py4b traced in blue, where Au occurs in the Co-Ni transition area with increased Se-Te-Pb-Bi in the Py4a. Au precipitation in the crystal lattice was associated with changing fluid conditions in the Co-Ni transition area with continued precipitation in the Ccp3/Py4b sulfide minerals. All concentrations are in ppm and elements with an * indicate maps

displayed to the 99th percentile to reduce inclusions. Notable values include Te* = 1,484 ppm, Au* = 51 ppm, Pb* = 94,513 ppm, and Bi* = 3,683 ppm. **B.** Inclusion-rich Apy where the Po inclusions are most favourable with Au with associated Ni-Ag-Pb-Tl-Bi. Inclusions have been traced in red. Notable values include Ni* = 3,191 ppm, Se* = 466 ppm, Mo* = 86 ppm, Ag* = 55 ppm, Au* = 12 ppm, Pb* = 43,679 ppm, Tl* = 139 ppm, and Bi* = 6,706 ppm.

Figure 12. LA-ICP-MS semi-quantitative element maps. **A.** Remobilized Au in Apy with dissolution. In this sample, Au occurs in fractures with increased Ag-Pb-Tl-Bi. Zonation is evident with Fe-Co-Ni-As-Se-Mo-Sb-Te and suggests changing fluid conditions. Inclusions have been traced in red. All concentrations are in ppm and elements with an * indicate maps displayed to the 99th percentile to reduce inclusions. Notable values include Mo* = 589 ppm, Pb* = 962 ppm, and Tl* = 40 ppm. **B.** Po4, traced in red, forming around a garnet in the wacke unit with elevated Co-Ni and microfractures with Pb-Tl-Bi.

Figure 13. Tukey box and whisker plot of element concentrations in Py and Po generations. Py2 is an early colloform pyrite in the subarkose unit, Po2 is found in the calc-silicate alteration, Py4a/b are found in the V_2 veins, Po4 is metamorphic associated, and Py6a/b are remobilized generations. Elements including Ni-Cu-Mo-Sb-Pb occur in greater abundance with Au-bearing sulfide minerals.

Figure 14 A. Zircon U-Pb geochronology of the granodiorite that intrudes the Porky Lake Group **B, C.** Outcrop photos showing granodiorite, traced, crosscutting the subarkosic unit.

Figure 15. Gold-related alteration and vein model of the Porky Main and Porky West deposits as related to the six stages of gold development as outlined in the text. **A.** *Stage 1.* Formation of V_1 veins in Assemblage A rocks and corresponding Po1-Py1-Ccp1. **B.** *Stage 2.* Juxtaposition of the

Porky Lake Group, subsequent intrusive event, and formation of early colloform Py2. **C.** *Stage 3.* Calc-silicate alteration and introduction of visible Au with Po2-Ccp2-Sp. **D.** *Stage 4.* V_2 veins and the introduction of Apy-Py4a/b-Po3-Ccp3. Using empirical calculations of chlorite and biotite associated with this vein generation, these veins formed at ~315ºC and ~3.1 kbar or 10.2 km depth. **E.** *Stage 5.* Peak metamorphism during D2 with Py5-Po4 aligned to foliation and subsequent folding of units during D3. **F.** *Stage 6.* Remobilization of Au from earlier sulfide minerals and growth of the youngest pyrite forming Py6a/b and eventual exhumation and erosion to present day. The scale shown in **F** refers to the present position of the system at the present day but should not be used to infer depth in **A** to **E**, or in the development of the youngest sulfide minerals in **F**. The shapes of the various sulfide minerals are taken from thin sections and should only be treated as schematic representations of the sulfide mineral phases.

References

Ansdell, K. M. 2005. Tectonic evolution of the Manitoba-Saskatchewan segment of the Paleoproterozoic Trans-Hudson Orogen, Canada. *Canadian Journal of Earth Sciences* 42: 741–759. doi: https://doi.org/10.1139/e05-035

Ansdell, K. M., and T. K. Kyser. 1992. Mesothermal gold mineralization in a Proterozoic greenstone belt; western Flin Flon Domain, Saskatchewan, Canada. *Economic Geology* 87: 1496–1524. doi: https://doi.org/10.2113/gsecongeo.87.6.1496

Ansdell, K. M., S. B. Lucas, K. Connors, and R. A. Stern. 1995. Kisseynew metasedimentary gneiss belt, Trans-Hudson orogen (Canada): Back-arc origin and collisional inversion. *Geology* 23: 1039. doi: https://doi.org/10.1130/0091-7613(1995)023<1039:KMGBTH>2.3.CO;2

Ashton, K. E. 1999. A proposed lithotectonic domainal re-classification of the southeastern Reindeer Zone in Saskatchewan. *In Summary of Investigations 1999, Volume 1, Saskatchewan Geological Survey, Sask. Energy Mines, Misc. Rep. 99-4.1*: 92–100.

Ashton, K. E., Lewry, J. F., Heaman, L. M., Hartlaub, R. P., Stauffer, M. R., and Tran, H. T. 2005: The Pelican Thrust Zone: basal detachment between the Archean Sask Craton and Paleoproterozoic Flin Flon–Glennie Complex, western Trans-Hudson Orogen; Can. J. Earth Sci., v42, no4, p685-706. doi: https://doi.org/10.1139/e04-035

Beaudin, D., C. A. Partin, K. Ansdell, V. Alexandre, R. Creaser, and R. B. Ickert. in revision. Multi-stage orogenic gold-mineralizing systematics at the Seabee Gold Operation, northern Saskatchewan, Canada: Constraints from pyrite chemistry and geochronology. *Mineralium Deposita*.

Beaudin, D., C. A. Partin, K. Ansdell, and P. Yang. 2024. Comparative lithology and alteration mineral chemistry of host rocks at the Seabee Gold Operation, northern Saskatchewan, Canada: Implications for a connected orogenic gold-mineralizing system. *Ore Geology Reviews* 166: 105950. doi: https://doi.org/10.1016/j.oregeorev.2024.105950

Bickford, M. E., W. R. V. Schmus, K. D. Collerson, and R. Macdonald. 1987. U-Pb zircon geochronology project: new results and interpretations. *In Summary of Investigations 1987, Saskatchewan Geological Survey, Sask. Energy Mines, Misc. Rep. 87-4*: 76–79.

Bucci, L., N. Mcnaughton, I. R. Fletcher, D. Groves, N. Kositcin, H. J. Stein, and S. Hagemann. 2004. Timing and Duration of High-Temperature Gold Mineralization and Spatially Associated Granitoid Magmatism at Chalice, Yilgarn Craton, Western Australia. *Economic Geology* 99: 1123–1144. doi: https://doi.org/10.2113/gsecongeo.99.6.1123

Cardenas-Vera, A., M. MacDonald, D. R. Lentz, and K. G. Thorne. 2023. Trace Element Characteristics of Pyrite and Arsenopyrite from the Golden Ridge Gold Deposit, New Brunswick, Canada: Implications for Ore Genesis. *Minerals* 13: 954. doi: https://doi.org/10.3390/min13070954

Cathelineau, M. 1988. Cation site occupancy in chlorites and illites as a function of temperature. *Clay Minerals* 23: 471–485. doi: https://doi.org/10.1180/claymin.1988.023.4.13

Chantler, C. T. 2000. Detailed tabulation of atomic form factors, photoelectric absorption and scattering cross section, and mass attenuation coefficients in the vicinity of absorption edges in the soft x-ray (Z=30-36, Z=60-89, E=0.1 keV-10 keV), addressing convergence issues of earlier work. *Journal of Physical and Chemical Reference Data* 29: 597–616. doi: https://doi.org/10.1063/1.1321055

Chen, L., X. Li, J. Li, A. H. Hofstra, Y. Liu, and A. E. Koenig. 2015. Extreme variation of sulfur isotopic compositions in pyrite from the Qiuling sediment-hosted gold deposit, West Qinling orogen, central China: an in situ SIMS study with implications for the source of sulfur. *Mineralium Deposita* 50: 643–656. doi: https://doi.org/10.1007/s00126-015-0597-9

Chiarenzelli, J. 1989. The Nistowiak and Guncoat Gneisses: Implications for the Tectonics of the Glennie and La Ronge Domains, Northern Saskatchewan, Canada. *Ph.D. thesis, Kansas, USA, University of Kansas*: 229.

Condon, D. J., B. Schoene, N. M. McLean, S. A. Bowring, and R. R. Parrish. 2015. Metrology and traceability of U–Pb isotope dilution geochronology (EARTHTIME Tracer Calibration Part I). *Geochimica et Cosmochimica Acta* 164: 464–480. doi: https://doi.org/10.1016/j.gca.2015.05.026

Cook, N. J., C. L. Ciobanu, D. Meria, D. Silcock, and B. Wade. 2013. Arsenopyrite-Pyrite Association in an Orogenic Gold Ore: Tracing Mineralization History from Textures and Trace Elements. *Economic Geology* 108: 1273–1283. doi: https://doi.org/10.2113/econgeo.108.6.1273

Corrigan, D., A. G. Galley, and S. Pehrsson. 2007. Tectonic evolution and metallogeny of the southwestern Trans-Hudson Orogen W. D. Goodfellow [ed.],. *in Mineral Deposits of Canada: A Synthesis of Major Deposit-Types, District Metallogeny, the Evolution of Geological Provinces, and Exploration Methods, Geological Association of Canada, Mineral Deposits Division* Special Publication 5: 881–902.

Corrigan, D., Z. Hajnal, B. Németh, and S. B. Lucas. 2005. Tectonic framework of a Paleoproterozoic arc-continent to continent-continent collisional zone, Trans-Hudson Orogen, from geological and seismic reflection studies. *Canadian Journal of Earth Sciences* 42: 421–434. doi: https://doi.org/10.1139/e05-025

Corrigan, D., S. Pehrsson, N. Wodicka, and E. De Kemp. 2009. The Palaeoproterozoic Trans-Hudson Orogen: a prototype of modern accretionary processes. *Geological Society, London, Special Publications* 327: 457–479. doi: https://doi.org/10.1144/SP327.19

Cox, S. F. 1999. Deformational controls on the dynamics of fluid flow in mesothermal gold systems. *Geological Society, London, Special Publications* 155: 123–140. doi: https://doi.org/10.1144/ GSL.SP.1999.155.01.10

Delaney, G. D. 1988. Bedrock Geological Mapping, Brownell Lake Area (Part of NTS 63M-4 and 63L-13). *In Summary of Investigation 1988, Saskatchewan Geological Survey; Saskatchewan Energy and Mines, Miscellaneous Report 88-4*.

Delaney, G. D. 1987. Bedrock Geological Mapping, Carruthers - Uskik Lakes Area (Part of NTS 63M-11 and -12). *In Summary of Investigations 1987, Saskatchewan Geological Survey; Saskatchewan Energy and Mines, Miscellaneous Report 87-4*.

Delaney, G. D. 1986. Bedrock Geological Mapping, Laonil Lake Area (Part of NTS 63M-11 and -12). *In Summary of Investigations 1986, Saskatchewan Geological Survey; Saskatchewan Energy and Mines, Miscellaneous Report 86-4*.

Delaney, G. D. 2016. Geology of the Pine Lake Greenstone Belt, Laonil - Uskik Lakes Area (Parts of NTS 63M -11 and 12); *Saskatchewan Geolocial Survey, Sask. Ministry of the Economy, Geoscience Map 2016-1, 1:50 000 scale map.*

Delaney, G. D., and S. A. Cutler. 1992. Geological Setting of the 'Santoy Lake' Gold Camp (Part of NTS 63M-11 and -12). *In Summary of Investigations 1992, Saskatchewan Geological Survey, Sask. Energy Mines, Misc. Rep. 92-4.*

Durocher, K. E. 1997. A study of the P-T-t fluid evolution of the Glennie Domain, Trans-Hudson Orogen. *Ph.D. Thesis, University of Saskatchewan*.

Durocher, K. E., S. A. Cutler, G. D. Delaney, and T. K. Kyser. 1992. Gold Occurrences in the 'Santoy Lake' Area, Glennie Domain, Trans-Hudson Orogen. *In Summary of Investigations 1992, Saskatchewan Geological Survey, Sask. Energy Mines, Misc. Rep. 92-4.*

Durocher, K. E., T. K. Kyser, and G. D. Delaney. 2001. Thermotectonic studies in the Paleoproterozoic Glennie domain, trans-Hudson orogen, Canada. *Precambrian Research* 109: 175–202. doi: https://doi.org/10.1016/S0301-9268(01)00144-9

Elliot, C. G. 1995. The Tabbernor fault and Proterozoic and Phanerozoic movements in Saskatchewan and Manitoba. *In LITHOPROBE Trans-Hudson Orogen Transect, 5th Transect Meeting, LITHOPROBE Secret, University of British Columbia, Report 48: 148-155.*

Foster, M. D. 1960. Interpretation of the composition of trioctahedral micas.

Gao, F., Y. Du, Z. Pang, Y. Du, F. Xin, and J. Xie. 2019. LA-ICP-MS Trace-Element Analysis of Pyrite from the Huanxiangwa Gold Deposit, Xiong'ershan District, China: Implications for Ore Genesis. *Minerals* 9: 157. doi: https://doi.org/10.3390/min9030157

Goldfarb, R. J., and D. I. Groves. 2015. Orogenic gold: Common or evolving fluid and metal sources through time. *Lithos* 233: 2–26. doi: https://doi.org/10.1016/j.lithos.2015.07.011

Goldfarb, R. J., D. I. Groves, and S. Gardoll. 2001. Orogenic gold and geologic time: a global synthesis. *Ore Geology Reviews* 18: 1–75. doi: https://doi.org/10.1016/S0169-1368(01)00016-6

Groves, D. I., R. J. Goldfarb, M. Gebre-Mariam, S. G. Hagemann, and F. Robert. 1998. Orogenic gold deposits: A proposed classification in the context of their crustal distribution and relationship to other gold deposit types. *Ore Geology Reviews* 13: 7–27. doi: https://doi.org/10.1016/S0169-1368(97)00012-7

Groves, D. I., M. Santosh, J. Deng, Q. Wang, L. Yang, and L. Zhang. 2020. A holistic model for the origin of orogenic gold deposits and its implications for exploration. *Mineralium Deposita* 55: 275–292. doi: https://doi.org/10.1007/s00126-019-00877-5

Groves, D. I., M. Santosh, R. J. Goldfarb, and L. Zhang. 2018. Structural geometry of orogenic gold deposits: Implications for exploration of world-class and giant deposits. *Geoscience Frontiers* 9: 1163–1177. doi: https://doi.org/10.1016/j.gsf.2018.01.006

Hastie, E. C. G., J. E. Gagnon, and I. M. Samson. 2018. The Paleoproterozoic MacLellan deposit and related Au-Ag occurrences, Lynn Lake greenstone belt, Manitoba: An emerging, structurally-controlled gold camp. *Ore Geology Reviews* 94: 24–45. doi: https://doi.org/10.1016/j.oregeorev.2018.01.016

Hastie, E. C. G., D. J. Kontak, and B. Lafrance. 2020. Gold Remobilization: Insights from Gold Deposits in the Archean Swayze Greenstone Belt, Abitibi Subprovince, Canada. *Economic Geology* 115: 241–277. doi: https://doi.org/10.5382/econgeo.4709

Helmy, H. M., C. Ballhaus, C. Wohlgemuth-Ueberwasser, R. O. C. Fonseca, and V. Laurenz. 2010. Partitioning of Se, As, Sb, Te and Bi between monosulfide solid solution and sulfide melt – Application to magmatic sulfide deposits. *Geochimica et Cosmochimica Acta* 74: 6174–6179. doi: https://doi.org/10.1016/j.gca.2010.08.009

Hoffman, P. F. 1988. United Plates of America, The Birth of a Craton: Early Proterozoic Assembly and Growth of Laurentia. *Annual Review of Earth and Planetary Sciences* 16: 543–603. doi: https://doi.org/10.1146/annurev.ea.16.050188.002551

Hou, L., H. Peng, J. Ding, J. Zhang, S. Zhu, S. Wu, Y. Wu, and H. Ouyang. 2016. Textures and In Situ Chemical and Isotopic Analyses of Pyrite, Huijiabao Trend, Youjiang Basin, China: Implications for Paragenesis and Source of Sulfur. *Economic Geology* 111: 331–353. doi: https://doi.org/10.2113/econgeo.111.2.331

Ispolatov, V., B. Lafrance, B. Dube, R. Creaser, and M. Hamilton. 2008. Geologic and Structural Setting of Gold Mineralization in the Kirkland Lake-Larder Lake Gold Belt, Ontario. *Economic Geology* 103: 1309–1340. doi: https://doi.org/10.2113/gsecongeo.103.6.1309

Kranidiotis, P., and W. H. MacLean. 1987. Systematics of chlorite alteration at the Phelps Dodge massive sulfide deposit, Matagami, Quebec. *Economic Geology* 82: 1898–1911. doi: https://doi.org/10.2113/gsecongeo.82.7.1898

Krogh, T. E. 1973. A low-contamination method for hydrothermal decomposition of zircon and extraction of U and Pb for isotopic age determinations. *Geochimica et Cosmochimica Acta* 37: 485–494. doi: https://doi.org/10.1016/0016-7037(73)90213-5

Lawley, C. J. M., R. A. Creaser, S. E. Jackson, Z. Yang, B. J. Davis, S. J. Pehrsson, B. Dubé, et al. 2015. Unraveling the Western Churchill Province Paleoproterozoic Gold Metallotect: Constraints from Re-Os Arsenopyrite and U-Pb Xenotime Geochronology and LA-ICP-MS Arsenopyrite Trace Element Chemistry at the BIF-Hosted Meliadine Gold District, Nunavut, Canada. *Economic Geology* 110: 1425–1454. doi: https://doi.org/10.2113/econgeo.110.6.1425

Lawley, C. J. M., X. M. Yang, D. Selby, W. Davis, S. Zhang, D. C. Petts, and S. E. Jackson. 2020. Sedimentary basin controls on orogenic gold deposits: New constraints from U-Pb detrital zircon and Re-Os sulphide geochronology, Lynn Lake greenstone belt, Canada. *Ore Geology Reviews* 126: 103790. doi: https://doi.org/10.1016/j.oregeorev.2020.103790

Leake, B. E., A. R. Woolley, C. E. S. Arps, W. D. Birch, M. C. Gilbert, J. D. Grice, F. C. Hawthorne, et al. 1997. Nomenclature of Amphiboles; Report of the Subcommittee on Amphiboles of the International Mineralogical Association Commission on New Minerals and Mineral Names. *Mineralogical Magazine* 61: 295–310. doi: https://doi.org/10.1180/minmag.1997.061.405.13

Lewry, J. F. 1977. The Geology of the Glennie Lake area, Saskatchewan (NTS Area 63-M-12). *Department of Mineral Resources, Saskatchewan Geological Survey*.

Lewry, J. F., and K. D. Collerson. 1990. The Trans-Hudson Orogen: Extent, Subdivision, and Problems. *Geological Association of Canada Special Paper, 37*: 1–14.

Lewry, J. F., D. J. Thomas, R. Macdonald, and J. Chiarenzelli. 1990. Structural relations in accreted terranes of the Trans-Hudson Orogen, Saskatchewan: telescoping in a collisional regime? Geological Association of Canada Special Paper.

Lucas, S. B., R. A. Stern, E. C. Syme, B. A. Reilly, and D. J. Thomas. 1996. Intraoceanic tectonics and the development of continental crust: 1.92–1.84 Ga evolution of the Flin Flon Belt, Canada. *Geological Society of America Bulletin* 108: 602. doi: https://doi.org/10.1130/0016-7606(1996)108<0602:ITATDO>2.3.CO;2

Ludwig, K. R. 2000. Decay constant errors in U–Pb concordia-intercept ages. *Chemical Geology* 166: 315–318. doi: https://doi.org/10.1016/S0009-2541(99)00219-3

Ludwig, K. R. 1998. On the Treatment of Concordant Uranium-Lead Ages. *Geochimica et Cosmochimica Acta* 62: 665–676. doi: https://doi.org/10.1016/S0016-7037(98)00059-3

Manitoba Geology Map Gallery. 2023. Website https://rdmaps.gov.mb.ca/Html5Viewer/index.html?viewer=MapGallery_Geology.MapGallery

Mao, S., R. Yang, Y. Qin, and J. Guo. 2009. Characteristics of gold-bearing mineral and occurrence of gold in the Yangshan gold field, Gansu Province. *Acta Petrologica Sinica* 25: 2776–2790.

Mathieu, L. 2019. Detecting magmatic-derived fluids using pyrite chemistry: Example of the Chibougamau area, Abitibi Subprovince, Québec. *Ore Geology Reviews* 114: 103127. doi: https://doi.org/10.1016/j.oregeorev.2019.103127

McCuaig, T. C., and R. Kerrich. 1998. P–T–t–deformation–fluid characteristics of lode gold deposits: evidence from alteration systematics. *Ore Geology Reviews* 12: 381–453. doi: https://doi.org/10.1016/S0169-1368(98)80002-4

McEwan, B. 2013. Summary of Geological Mapping of the Santoy Mine Area during the Summer of 2012. *In Internal Report. Claude Resources Inc.*: 24.

McLean, N. M., D. J. Condon, B. Schoene, and S. A. Bowring. 2015. Evaluating uncertainties in the calibration of isotopic reference materials and multi-element isotopic tracers (EARTHTIME Tracer Calibration Part II). *Geochimica et Cosmochimica Acta* 164: 481–501. doi: https://doi.org/10.1016/j.gca.2015.02.040

McNicoll, V. J., G. D. Delaney, R. R. Parrish, and L. M. Heaman. 1992. U - Pb Determinations From the Glennie Lake Domain, Trans - Hudson Orogen, Saskatchewan. *In Radiogenic Age and Isotopic Studies: Report 6, Geol. Surv. Can., Pap. 92-2, p57-72*

Meffre, S., R. R. Large, J. A. Steadman, D. D. Gregory, A. S. Stepanov, V. S. Kamenetsky, K. Ehrig, and R. J. Scott. 2016. Multi-stage enrichment processes for large gold-bearing ore deposits. *Ore Geology Reviews* 76: 268–279. doi: https://doi.org/10.1016/j.oregeorev.2015.09.002

Mériaud, N., and M. Jébrak. 2017. From intrusion-related to orogenic mineralization: The Wasamac deposit, Abitibi Greenstone Belt, Canada. *Ore Geology Reviews* 84: 289–308. doi: https://doi.org/10.1016/j.oregeorev.2017.01.021

Meyer, M. T., M. E. Bickford, and J. F. Lewry. 1992. The Wathaman Batholith: an Early Proterozoic continental arc in the Trans-Hudson Orogen, Canada. *Geol. Soc. Am. Bull., v104*: 1073–1085. doi: https://doi.org/10.1130/0016-7606(1992)104<1073:TWBAEP>2.3.CO;2

Morelli, R. M., R. A. Creaser, D. Selby, D. J. Kontak, and R. J. Horne. 2005. Rhenium-Osmium Geochronology of Arsenopyrite in Meguma Group Gold Deposits, Meguma Terrane, Nova Scotia, Canada: Evidence for Multiple Gold-Mineralizing Events. *Economic Geology* 100: 1229–1242. doi: https://doi.org/10.2113/gsecongeo.100.6.1229

Morelli, R., and K. MacLachlan. 2012. Saskatchewan Gold: Mineralization Styles and Mining History. *Sask Ministry of Energy and Resources Rep 262*: 171.

Pouchou, J. L., and F. Pichoir. 1984. New Model for Quantitative X-Ray Microanalysis. Part II: Application to In-Depth Analysis of Heterogeneous Samples. *Recherche Aerospatiale (English Edition)*: 47–65.

Poulsen, K. H., K. D. Card, and J. M. Franklin. 1992. Archean Tectonic and Metallogenic Evolution of the Superior Province of the Canadian Shield. *Precambrian Research* 58: 25–54. doi: https://doi.org/10.1016/0301-9268(92)90111-Z

Rubingh, K. E. L., B. Lafrance, and H. L. Gibson. 2024. The Snow Lake Deposits in Manitoba, Canada: Formation of Metamorphosed Amphibolite Facies Orogenic Gold Deposits During a Progressive and Prograde Orogenic Event. *Economic Geology* 119: 421–444. doi: https://doi.org/10.5382/econgeo.5048

Saskatchewan GeoATLAS Mapping. 2023. Website https://gisappl.saskatchewan.ca/Html5Ext/index.html?viewer=GeoAtlas [accessed 1 March 2024].

Schneider, D. A., M. T. Heizler, M. E. Bickford, G. L. Wortman, K. C. Condie, and S. Perilli. 2007. Timing constraints of orogeny to cratonization: Thermochronology of the Paleoproterozoic Trans-Hudson orogen, Manitoba and Saskatchewan, Canada. *Precambrian Research* 153: 65–95. doi: https://doi.org/10.1016/j.precamres.2006.11.007

Schultz, D. J. 1996. The Fluid History of the Seabee Mesothermal Gold Deposit Northern Saskatchewan. *M.Sc. Thesis, University of Saskatchewan*.

Sibson, R. H., F. Robert, and K. H. Poulsen. 1988. High-angle reverse faults, fluid-pressure cycling, and mesothermal gold-quartz deposits. *Geology* 16: 551. doi: https://doi.org/10.1130/0091-7613(1988)016<0551:HARFFP>2.3.CO;2

Sillitoe, R. H., and J. F. H. Thompson. 1998. Intrusion-Related Vein Gold Deposits: Types, Tectono-Magmatic Settings and Difficulties of Distinction from Orogenic Gold Deposits. *Resource Geology* 48: 237–250. doi: https://doi.org/10.1111/j.1751-3928.1998.tb00021.x

SRK Consulting. 2021. NI 43-101 Technical Report for the Seabee Gold Operation, Saskatchewan, Canada.

Stauffer, M. R. 1984. Manikewan: An early proterozoic ocean in central Canada, its igneous history and orogenic closure. *Precambrian Research* 25: 257–281. doi: https://doi.org/10.1016/0301-9268(84)90036-6

Syme, E. C., and A. H. Bailes. 1993. Stratigraphic and tectonic setting of early Proterozoic volcanogenic massive sulfide deposits, Flin Flon, Manitoba. *Economic Geology* 88: 566–589. doi: https://doi.org/10.2113/gsecongeo.88.3.566

Tait, K. T., L. F. White, E. C. G. Hastie, D. C. Crabtree, H. L. Gibson, R. L. Sherlock, J. A. Petrus, and B. Langelier. 2023. Nanoscale Distribution of Elements in Gold: Examples from Contrasting Deposit Types. *The Canadian Journal of Mineralogy and Petrology* 61: 433–444. doi: https://doi.org/10.3749/2200024

Tomkins, A. G., and J. A. Mavrogenes. 2001. Redistribution of Gold within Arsenopyrite and Löllingite during Pro- and Retrograde Metamorphism: Application to Timing of Mineralization. *Economic Geology* 96: 525–534. doi: https://doi.org/10.2113/gsecongeo.96.3.525

Tomkins, A. G., D. R. M. Pattison, and E. Zaleski. 2004. The Hemlo Gold Deposit, Ontario: An Example of Melting and Mobilization of a Precious Metal-Sulfosalt Assemblage during Amphibolite Facies Metamorphism and Deformation. *Economic Geology* 99: 1063–1084. doi: https://doi.org/10.2113/gsecongeo.99.6.1063

Tourigny, G., G. Chi, C. Yuhasz, R. Olson, J. Berger, and J. Soloman. 2004. Structural Controls and Temperature-Pressure Conditions of Gold-bearing Quartz Vein Systems at the Seabee Mine, Northern Saskatchewan. In Summary of Investigations 2004, Volume 2, Saskatchewan Geological Survey, Sask. Industry Resources, Misc. Rep. 2004-4.2, CD-ROM, Paper A-2, 18p.

Uchida, E., S. Endo, and M. Makino. 2007. Relationship Between Solidification Depth of Granitic Rocks and Formation of Hydrothermal Ore Deposits. *Resource Geology* 57: 47–56. doi: https://doi.org/10.1111/j.1751-3928.2006.00004.x

Van Schmus, W. R., M. E. Bickford, J. F. Lewry, and R. Macdonald. 1987. U–Pb geochronology in the Trans-Hudson Orogen, northern Saskatchewan, Canada. *Canadian Journal of Earth Sciences* 24: 407–424. doi: https://doi.org/10.1139/e87-043

Vikent'eva, O., and I. Vikentev. 2016. Occurrence modes of As, Sb, Te, Bi, Ag in sulfide assemblages of gold deposits of the Urals. *IOP Conference Series: Materials Science and Engineering* 123: 012028. doi: https://doi.org/10.1088/1757-899X/123/1/012028

Whitney, D. L., and B. W. Evans. 2010. Abbreviations for names of rock-forming minerals. *American Mineralogist* 95: 185–187. doi: https://doi.org/10.2138/am.2010.3371

Willson, J. R. 2010. Minerals and Rocks. BookBoon Pres.

Witvoet, L. 2023. Petrological and Geochemical Comparison of the Eisler Intrusive Suite and the Laonil Lake Intrusive Complex Glennie Domain Northern Saskatchewan. *M.Sc. Thesis, University of Saskatchewan*.

Wood, C. 2016. Structural Study of the Auriferous Santoy Shear Zone Northeastern Glennie Domain. *M.Sc. Thesis, University of Regina*.

York, D., N. M. Evensen, M. L. Martínez, and J. De Basabe Delgado. 2004. Unified equations for the slope, intercept, and standard errors of the best straight line. *American Journal of Physics* 72: 367–375. doi: https://doi.org/10.1119/1.1632486

Zang, W., and W. S. Fyfe. 1995. Chloritization of the hydrothermally altered bedrock at the Igarapé Bahia gold deposit, Carajas, Brazil. *Mineralium Deposita*. doi: https://doi.org/10.1007/BF00208874

Zhang, P., X.-W. Huang, B. Cui, B.-C. Wang, Y.-F. Yin, and J.-R. Wang. 2016. Re-Os isotopic and trace element compositions of pyrite and origin of the Cretaceous Jinchang porphyry Cu-Au deposit, Heilongjiang Province, NE China. *Journal of Asian Earth Sciences* 129: 67–80. doi: https://doi.org/10.1016/j.jseaes.2016.06.004

Zwanzig, H. 2000. Geochemistry and tectonic framework of the Kisseynew Domain-Lynn Lake belt boundary (part of NTS 63P/13). *In Report of Activities 2000, Manitoba Industry, Trade and Mines, Manitoba Geological Survey*: 91–96.

Table 1. Sulfide mineral phase and average composition (ppm); nd = not detected. Sulfide phases marked with an * indicate data from microprobe analyses (Supplementary Data File A) whereas those without an * are from LA-ICP-MS data (Supplementary Data File B).

Sulfide Generation	Association	Co	Ni	Cu	As	Se	Mo	Ag	Sb	Te	Au	Total Pb	Tl	Bi
Po1*	V_1 veins	2,300	1,200	nd	400	400	300	200	nd	nd	nd	3,500	nd	nd
Py1*	V_1 veins	600	900	300	800	500	nd	400	nd	nd	nd	5,600	nd	nd
Py2	Early colloform pyrite	1	5,074	1,501	20,562	152	14	564	30	1	nd	17,832	169	27
Po2	Calc-silicate alteration	14	254	61	42	24	nd	0	15	3	nd	1	nd	4
Py3*	Calc-silicate alteration	700	3,700	nd	400	nd	nd	400	nd	nd	nd	4,200	nd	nd
Po3*	V_2 veins	533	233	33	267	nd	nd	233	nd	nd	nd	3,233	nd	nd
Py4a	V_2 veins	1	4,157	1,106	13,151	151	5	244	11	24	2	11,465	58	55
Py4b	V_2 veins	nd	373	31,939	1,644	148	nd	50	3	1	nd	1,393	1	8
Apy	V_2 veins	370	645	353	1,691,653	33	1	nd	130	26	nd	5	nd	10
Po4	Metamorphism associated	503	2,015	44	220	45	0	2	9	9	nd	9	nd	10
Py6a	Brittle deformation	7	776	18	121	40	nd	1	nd	4	nd	119	21	nd
Py6b	Brittle deformation	nd	2,442	1,057	7,496	64	4	247	12	2	2	11,478	57	nd

Table 2. Geochronology results. Full dataset in Supplementary Data File C: U-Pb Geochronology Supplementary Data.

Zircon fraction	Composition				Isotopic Ratios								Dates (Ma)							
	Th/U	Pb* (pg)	Pbc (pg)	Pb*/Pbc	$^{206}Pb/^{204}Pb$	$^{208}Pb/^{206}Pb$	$^{206}Pb/^{238}U$	±2σ %	$^{207}Pb/^{235}U$	±2σ %	$^{207}Pb/^{206}Pb$	±2σ %	$^{206}Pb/^{238}U$	±2σ abs	$^{207}Pb/^{235}U$	±2σ abs	$^{207}Pb/^{206}Pb$	±2σ abs	Corr. Coef.	% disc
z10	0.72	20.2	4.34	5	280	0.208	0.348	0.44	5.58	1.8	0.1163	1.5	1925	7.4	1913	16	1899	28	0.742	-1.36
z15	0.61	18.1	0.29	62	3618	0.176	0.33263	0.19	5.188	0.27	0.11316	0.14	1851.2	3.1	1850.6	2.3	1850	2.7	0.848	-0.06
z03	0.58	35.1	0.53	66	3837	0.167	0.33155	0.13	5.164	0.23	0.11301	0.14	1846	2.1	1846.7	1.9	1847.5	2.6	0.817	0.09
z08	0.49	54.2	0.37	148	8793	0.141	0.33132	0.09	5.159	0.15	0.112981	0.088	1844.9	1.4	1845.9	1.3	1847.1	1.7	0.83	0.12
z09	0.54	33.9	0.32	104	6140	0.157	0.33111	0.11	5.1477	0.18	0.11281	0.11	1843.8	1.8	1844	1.5	1844.3	2	0.808	0.03
z14	0.51	38.2	0.34	112	6655	0.149	0.33067	0.11	5.136	0.2	0.11271	0.1	1841.7	1.8	1842.2	1.7	1842.7	2	0.895	0.06
z07	0.61	56.8	0.47	121	6990	0.176	0.33063	0.085	5.1365	0.15	0.11272	0.094	1841.5	1.4	1842.2	1.3	1843	1.8	0.772	0.08
z04	0.49	46.3	0.58	80	4764	0.143	0.33053	0.094	5.1384	0.18	0.1128	0.13	1841	1.5	1842.5	1.5	1844.2	2.5	0.673	0.18
z11	0.45	115	0.33	355	21270	0.131	0.33047	0.08	5.1315	0.14	0.112669	0.07	1840.7	1.3	1841.3	1.2	1842.1	1.4	0.882	0.08
z21	0.4	28	1.1	26	1571	0.116	0.3302	0.14	5.131	0.36	0.11274	0.28	1839.4	2.2	1841.2	3	1843.2	5.1	0.702	0.21
z12	0.51	27.8	0.59	47	2800	0.148	0.33011	0.15	5.132	0.28	0.1128	0.19	1839	2.4	1841.4	2.4	1844.2	3.6	0.722	0.29
z13	0.61	29.2	0.4	73	4259	0.177	0.33003	0.13	5.125	0.2	0.11268	0.13	1838.6	2.1	1840.3	1.7	1842.3	2.4	0.785	0.21
z19	0.41	30.1	0.39	76	4635	0.119	0.33	0.12	5.1201	0.19	0.11258	0.11	1838.5	1.8	1839.4	1.6	1840.7	2.2	0.811	0.12

z16	0.43	94.5	0.59	160	9664	0.124	0.32992	0.078	5.1235	0.14	0.112681	0.082	1838	1.2	1840	1.2	1842.3	1.6	0.847	0.23
z20	0.65	14.6	0.34	43	2487	0.188	0.32846	0.24	5.089	0.37	0.11241	0.26	1831	3.8	1834.2	3.1	1837.9	4.8	0.695	0.38
z06	0.43	37.4	0.58	64	3871	0.125	0.32816	0.11	5.069	0.2	0.11209	0.13	1829.5	1.7	1831	1.7	1832.8	2.5	0.77	0.18
z05	0.66	24.2	3.59	7	405	0.192	0.3271	0.31	5.03	1.3	0.1116	1.1	1824.5	4.9	1824	11	1824	20	0.726	-0.01

Table 3. Comparison between associated Au features between the Porky, Fisher, Santoy, and Seabee deposits.

	Porky	**Fisher**	**Santoy**	**Seabee**
Vein generations	At least 3	At least 3	At least 3	At least 3
Main alteration	Calc-silicate (Di–Ser–Pl–Bt–Ms–Kfs–Cal–Aug–Ttn–Ap ± Chl)	Calc-silicate (Di–Kfs–Ab–Act–Ser–Bt–Chl–Czo ± Ap–Ttn)	Calc-silicate (Di–Kfs–Ab–Act–Ser–Bt–Chl–Czo ± Ap–Ttn)	Carbonate-Tur ± sericite ± chlorite
Dominant Au-associated minerals	Py-Po-Ccp-Apy ± Sp-Gn	Py-Po-Ccp ± Apy	Po-Py-Ccp-Apy-Sp ± Sch-Gn-Hem-Mol-Apy-Mag	Py-Po-Ccp ± Apy
Forms of Au	Visible, fracture-hosted, inclusion-hosted, and minor lattice-bound Au	Visible, inclusion-hosted, and minor lattice-bound Au	Visible, inclusion-hosted, and fracture-hosted Au	Visible, fracture-hosted, and minor lattice-bound Au
Associated elements	As-Cu-Co–Ni-Ag-Pb-Zn-Sb-Bi-Te	Co–Ni–Cu–Zn–Pb–As–Ag–Te–W–Bi	Co–Ni–Cu–Zn–Pb–As–Ag–Te–W–Bi	As-Cu-Ag-Sb-Bi-Te
Main Au mineralization conditions	~315 °C, ~3.1 kbar	~310–320 °C, ~3 kbar	~360 °C, 2–3 kbar	~370 °C, 1.1–2.5 kbar
Structural control on Au	Shear zones, fractures, boudinaged veins and alteration, and remobilization	Shear zones, remobilized	Shear zones, pressure shadows, boudinaged veins and alteration, and remobilized	Shear zones, brittle fractures, remobilized

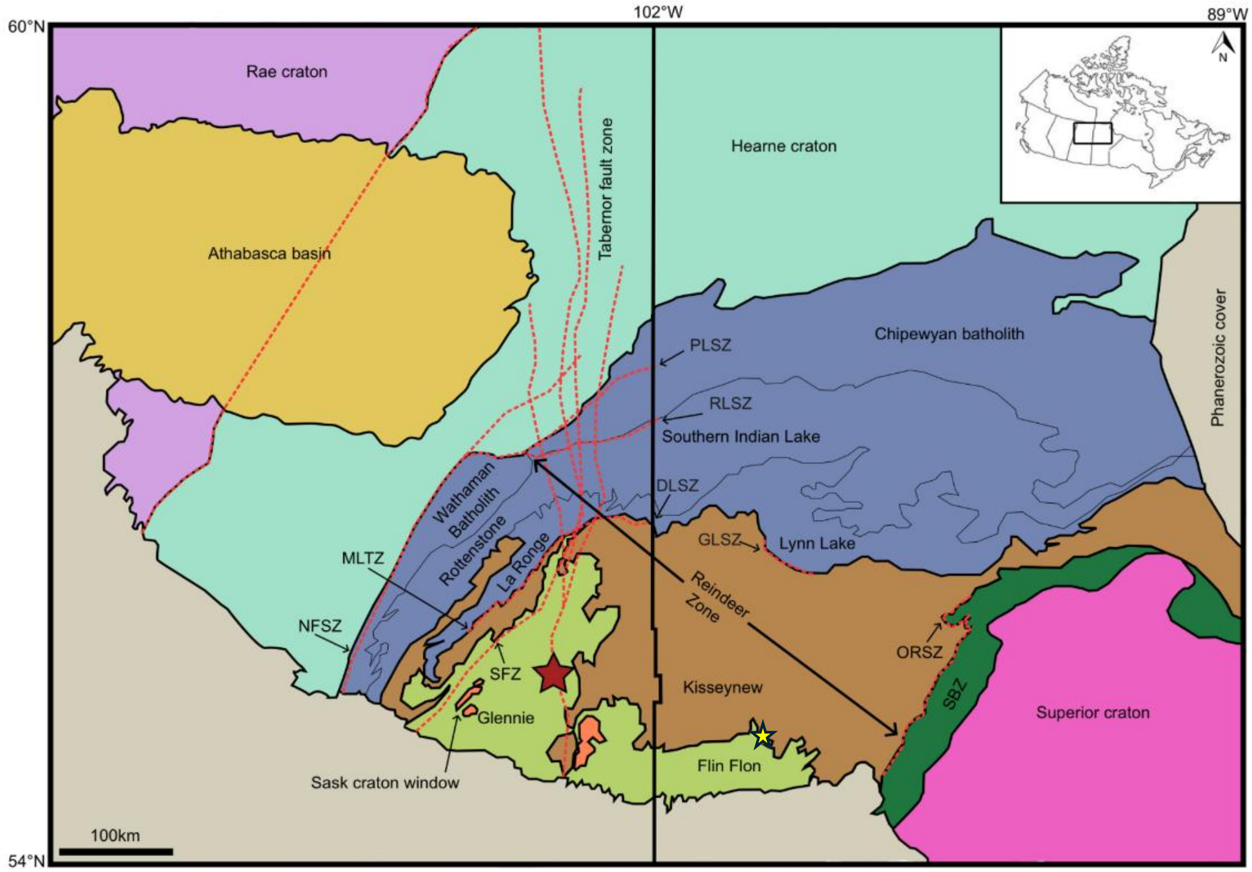

Figure 1. Trans-Hudson orogen subdivisions of northern Saskatchewan and Manitoba. The red star indicates the Seabee Gold Operation. Map modified after Corrigan et al. (2007) with updated domain boundaries with the most recent map data sourced from the Saskatchewan GeoAtlas (2023) and Manitoba Geology Map Gallery (2023). The yellow star indicates the New Britannia Mine in the Flin Flon Domain and was included as this study compares gold mineralization in that area. Meliadine Gold District is also referenced but is outside the map constraints and is north of Rankin Inlet, Nunavut. Major regional structures include RLSZ = Reilly Lake shear zone, DLSZ = Duck Lake shear zone, MLTZ = McLennan Lake tectonic zone, NFSZ = Needle Falls shear zone, PLSZ = Parker Lake shear zone, SFZ = Stanley fault zone, ORSZ = Owl River shear zone, GLSZ = Granville Lake structural zone, and SBZ = Superior boundary zone.

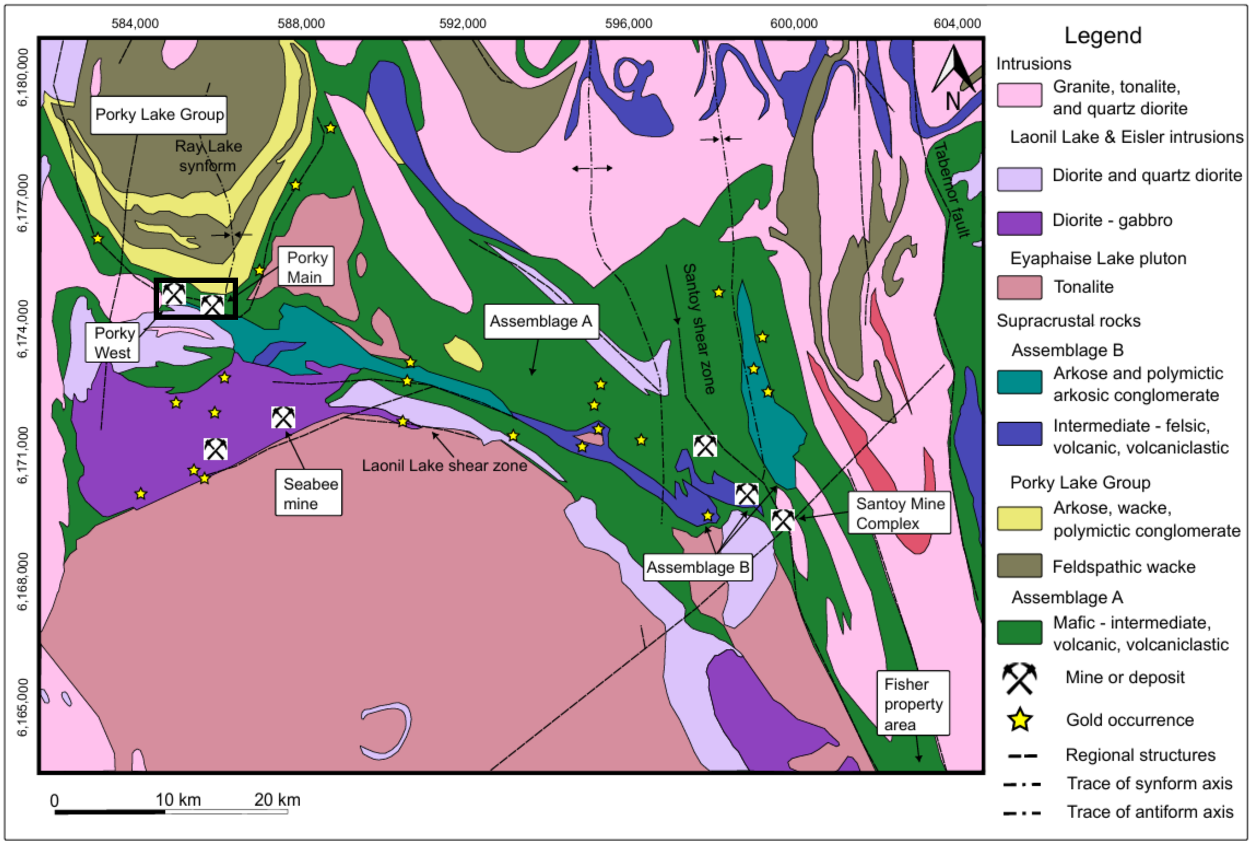

Figure 2. Simplified 1:250,000 geological map of the Pine Lake greenstone belt and area surrounding the Seabee Gold Operation, northern Saskatchewan, NAD83 Zone 13N with the most recent map data sourced from the Saskatchewan GeoATLAS Mapping (2023); gold occurrences (yellow star) from SRK Consulting (2017). Water bodies have been omitted for clarity. The study area is indicated by the black box near the Porky deposits.

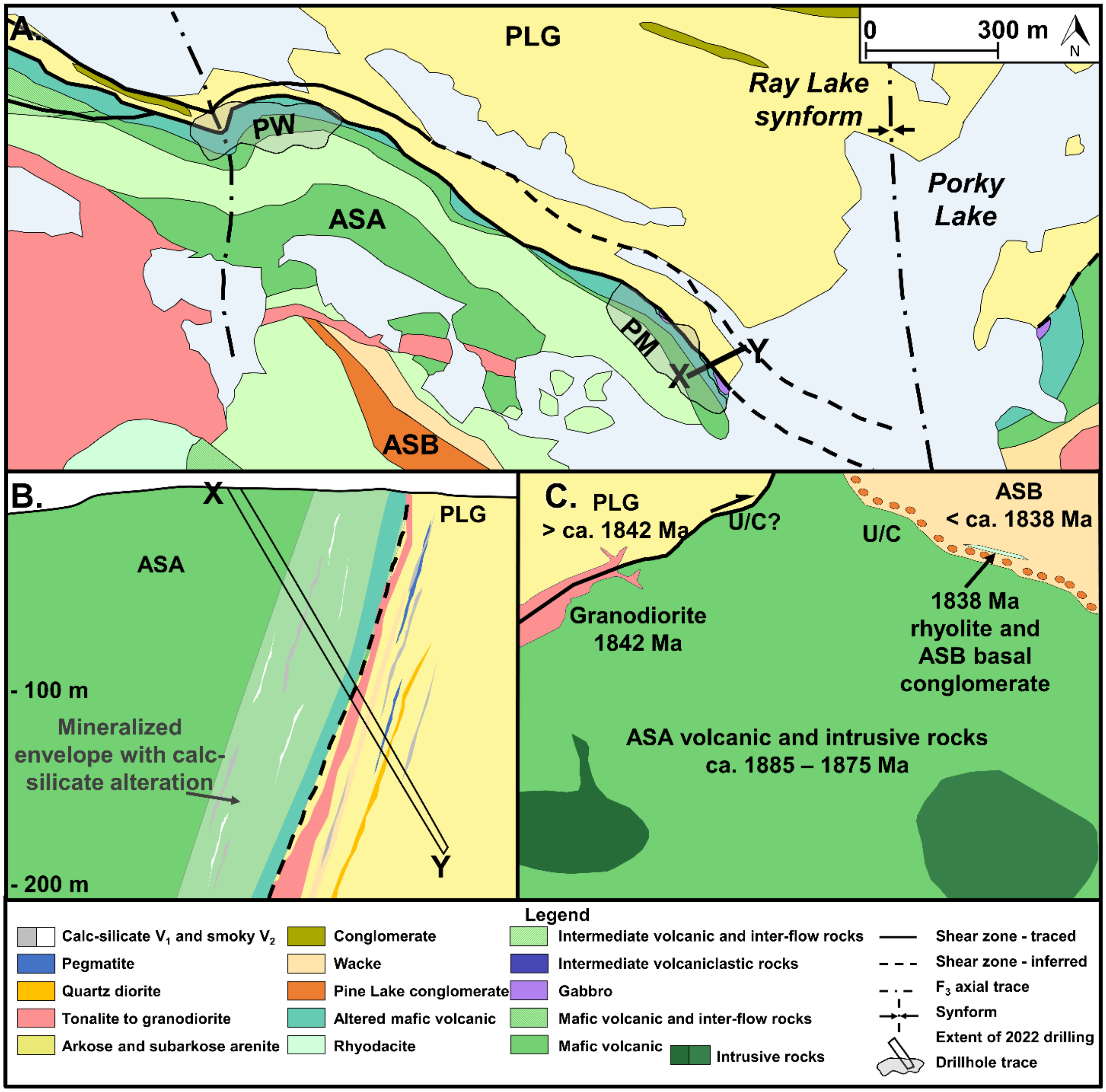

Figure 3. A. Geological map of the Porky West and Porky Main deposits along a mineralized shear zone. PLG = Porky Lake Group, ASA = Assemblage A, ASB = Assemblage B, PW = Porky West, PM = Porky Main. Map data based on Saskatchewan GeoATLAS Mapping (2023). **B.** The schematic cross-section is based on a drillhole plunging from X-Y. **C.** Simplified stratigraphy of the area showing the relationship with the Porky Lake Group and Assemblage B with Assemblage A.

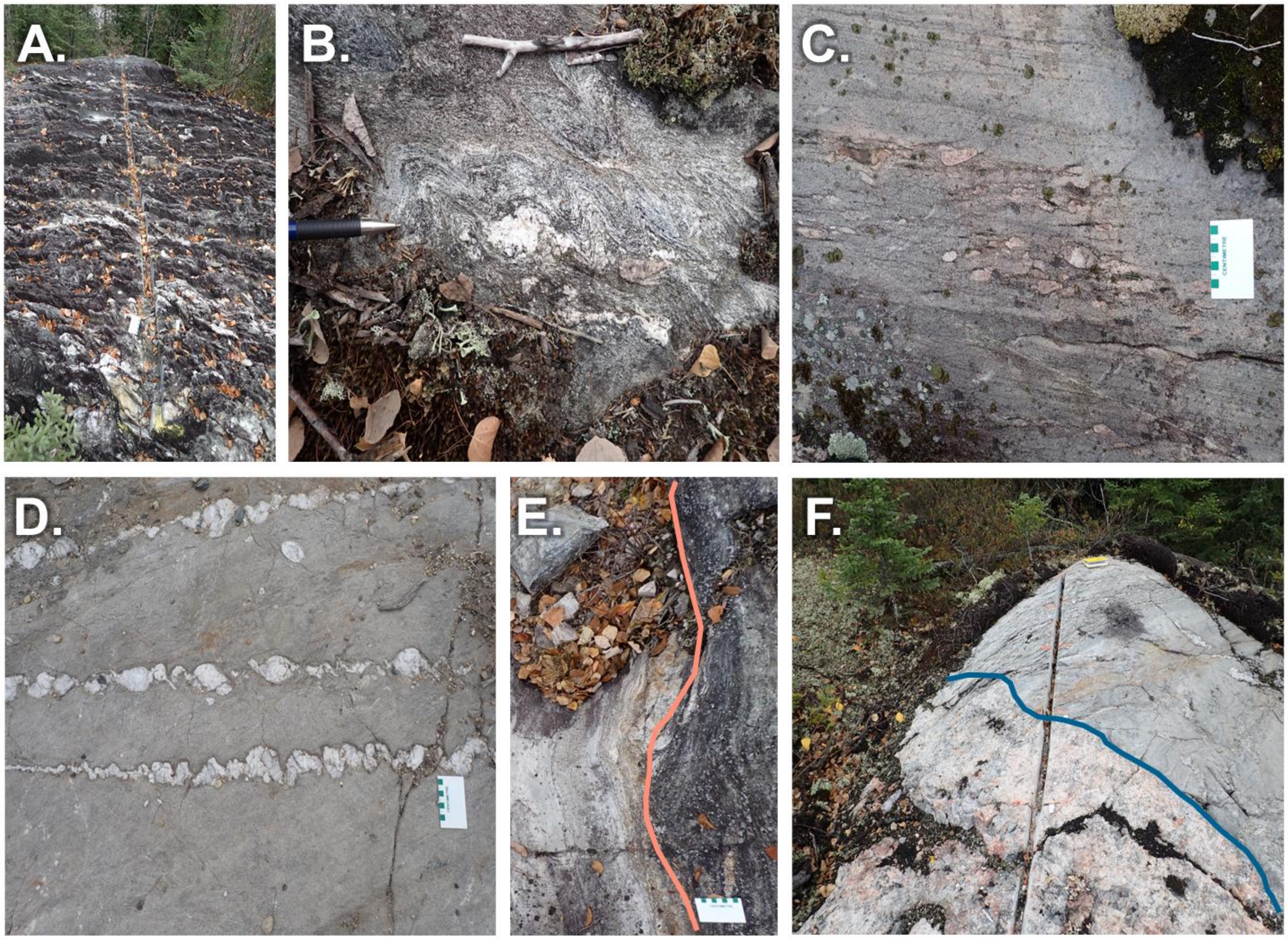

Figure 4. Rock units present at the Porky Main and Porky West deposits. **A.** Mafic volcanic rock along a mineralized shear zone with V_1 veins. **B.** Folded V_1 veins in an intermediate rock. **C.** Conglomerates in the subarkosic unit that has clasts aligned to foliation. **D.** Rotated and boudinaged V_2 veins with subsequent folding in the subarkosic unit. **E.** Granodiorite (left) and mafic volcanic (right) contact. **F.** Pegmatite (bottom) cutting the subarkosic unit (top).

Figures for Dixon et al.

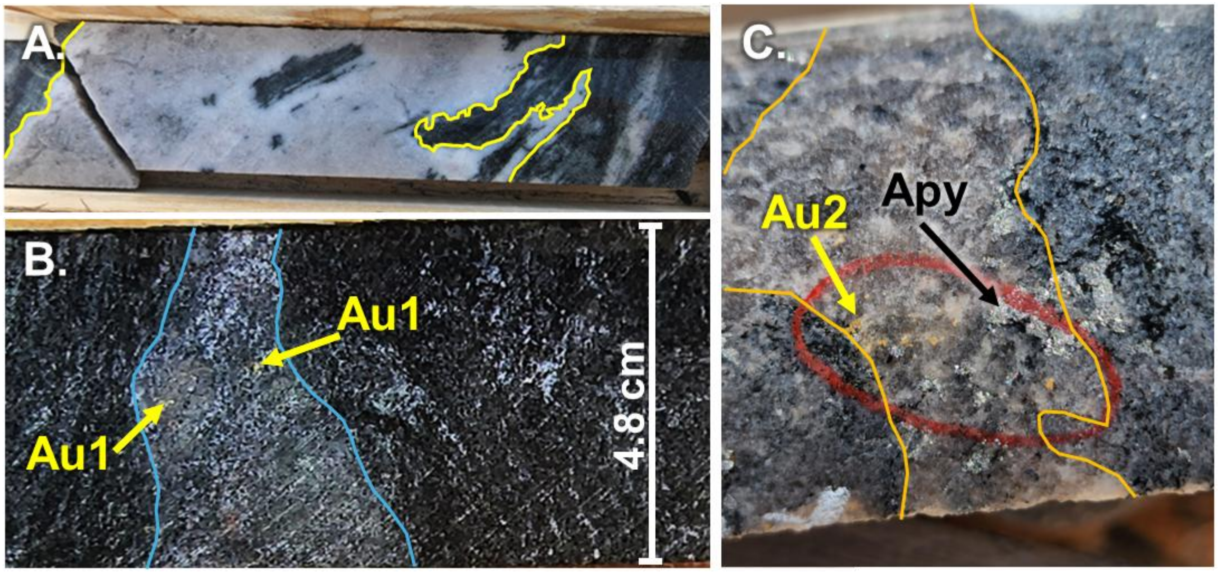

Figure 5. Calc-silicate alteration, veins, and host lithologies in drillcore. The alteration and veins commonly have irregular margins and are semi-concordant and concordant to foliation. **A.** Calc-silicate V_1 veins in a mafic volcanic rock. **B.** Pervasive calc-silicate alteration in an altered mafic volcanic rock. **C.** V_2 veins with arsenopyrite (Apy) and visible gold are focused along the vein margins in the subarkosic unit.

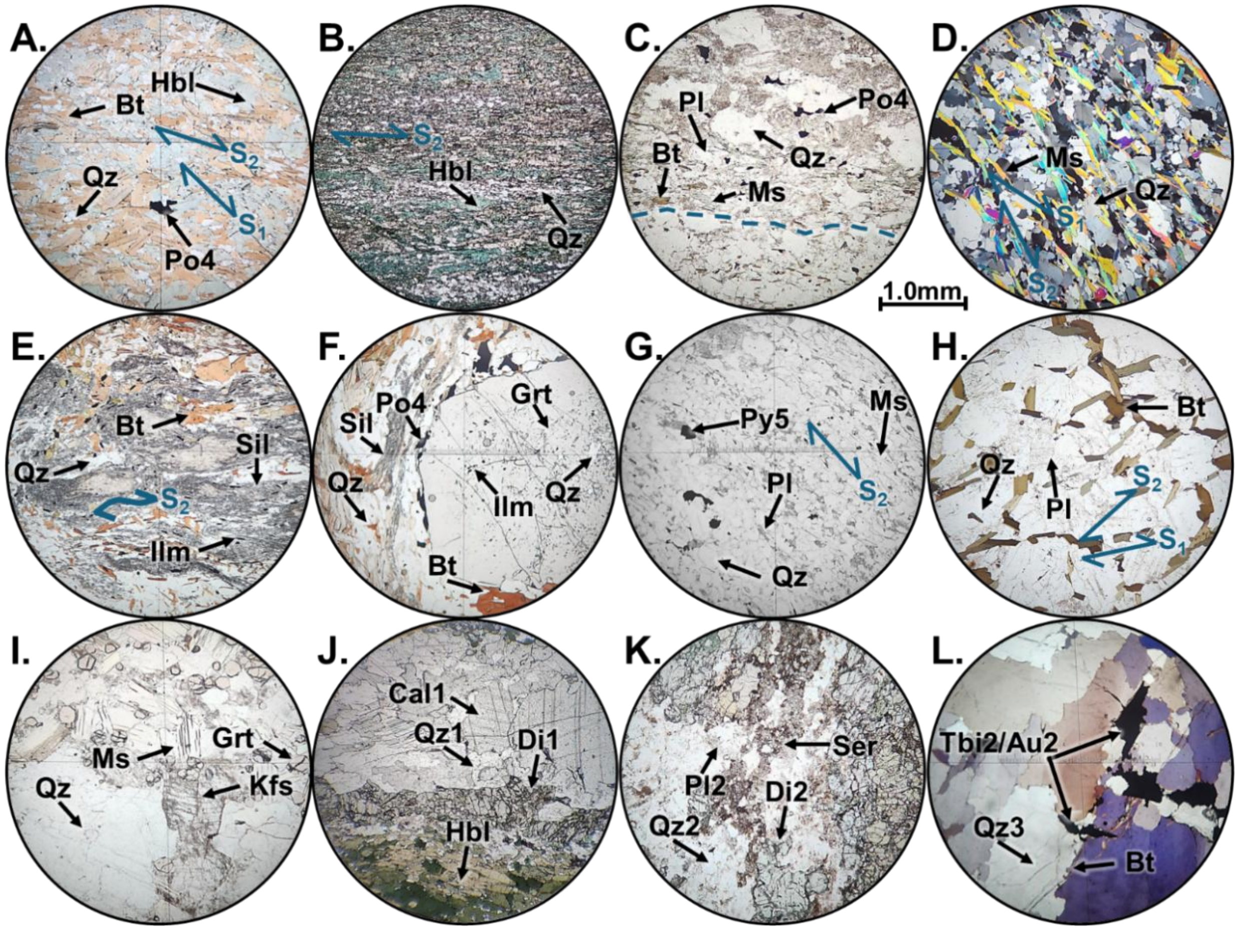

Figure 6. Photomicrographs of rock units (unmineralized) from the study area. Field of view (FOV) = 4.5 mm. **A.** Plane polarized light (PPL) of mafic volcanic unit with S_1/S_2 foliation. **B.** PPL of intermediate volcanic unit with S_2 foliation defined primarily by Hbl-Bt-Qz. **C.** PPL of conglomerate in the subarkosic unit. **D.** Cross-polarized light (XPL) of subarkosic unit; S1/S2 foliation defined by Ms and Qz. **E.** PPL of wacke with S_2 foliation defined by fibrolite and Bt. **F.** PPL of same wacke showing garnet with Po4 forming around the rim. **G.** PPL of porphyritic granodiorite with Py5 grains; S_2 foliation defined by Pl-Ms-Qz. This unit was used for geochronology to constrain the age of the Porky Lake Group. **H.** PPL of quartz diorite; S_1/S_2 foliation defined by alignment of Bt. **I.** PPL of early K-feldspar pegmatite with Grt. **J.** PPL of calc-silicate V_1 vein on the margin of the mafic volcanic unit. **K.** Pervasive calc-silicate alteration with Ser-Di2-Pl2-Qz2. **L.** XPL in V_2 vein showing grain boundaries with visible Tbi2/Au2 grains.

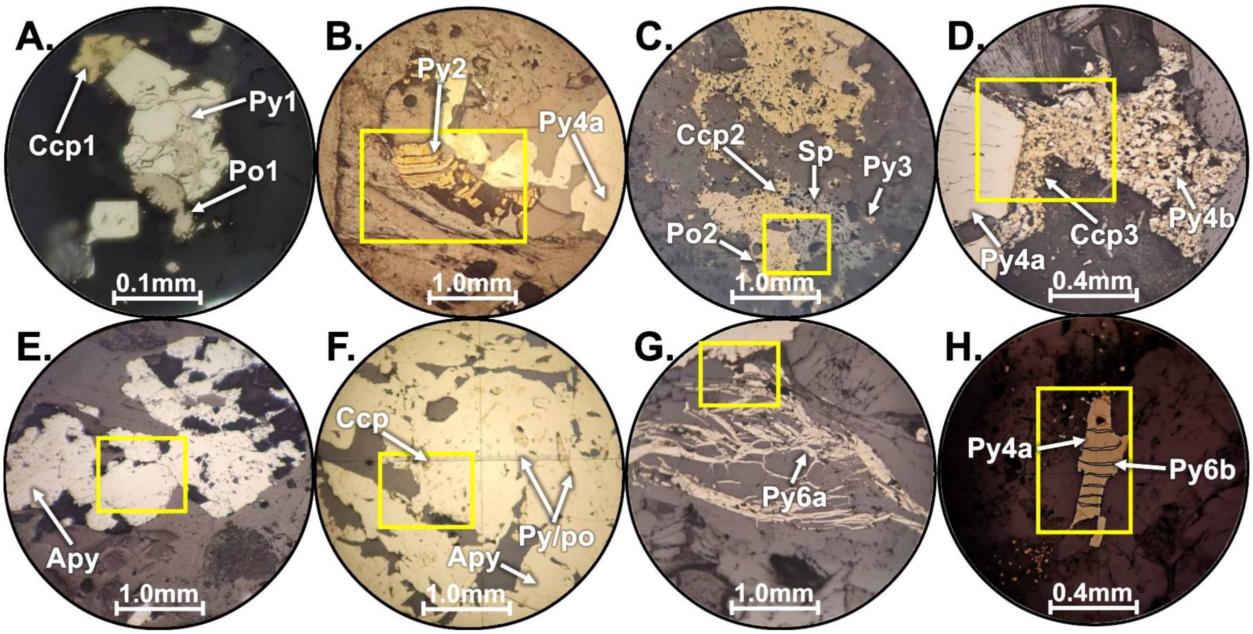

Figure 7. Photomicrographs of representative sulfide mineral generations (reflected light); yellow boxes indicate areas used for LA-ICP-MS. The sulfide mineral shapes were used to represent the sulfide generations in Fig. 14. **A.** Trace pyrrhotite-pyrite-chalcopyrite (Po1-Py1-Ccp1) of the V_1 veins. **B.** Early colloform Py2 occurs as a trace sulfide in the subarkosic unit with Py4a when associated with V_2 veins. **C.** Porous Po2-Ccp2-Sp of the pervasive calc-silicate alteration in the mafic volcanic unit; also associated with Py3-Gn. **D.** Euhedral Py4a and disseminated Ccp3-Py4b associated with V_2 veins. **E.** Anhedral Apy with dissolution and gold forming in microfractures. **F.** Inclusion-rich Apy in the pegmatite unit. Metamorphic-associated Po4 (Fig. 6F–G) is associated with Py5 in the intrusive units. **G.** Remobilized Py6a occurs around brecciated Qt-Ms-Bt grains. **H.** Py6b with crystal lattice controlled exsolution and subparallel horizontal bands from an earlier Py4a. The Py6b has been traced for clarity.

Unit	Minerals	Albite-diopside veins (V_1)		Calc-silicate alteration	Smoky quartz veins (V_2)	Peak metamorphism (wall rock)	Remobilization
	Hbl					Hbl	
	Bt			Bt1	Bt2	Bt3	
	Qz	Qz1		Qz2	Qz3	Qz4	
	Pl	Pl1		Pl2		Pl3	
	Di	Di1		Di2			
	Ser			Ser			
	Ms			Ms1			
	Ap			Ap1			
	Ttn			Ttn			
	Kfs			Kfs1			
Assemblage A	Cal	Cal1		Cal2			
	Chl				Chl		
	Po	Po1		Po2		Po4	
	Py	Py1		Py3			
	Apy				Apy		
	Ccp	Ccp1		Ccp2			
	Mag	Mag1				Mag2	
	Au			Au1	Au2		Au3
	Tbi			Tbi1	Tbi2		
	Sp			Sp			
	Gn			Gn			
	Qz				Qz3	Qz4	
	Ms					Ms2	
	Pl			Pl2		Pl3	
	Bt					Bt3	
	Kfs				Kfs2	Kfs3	
	Sil					Sil	
	Grt					Grt	
	Ap				Ap2		
	Mnz						Mnz
Porky Lake Group	Rt						Rt
	Cei						Cei
	Apy				Apy		
	Po				Po3	Po4	
	Py		Py2?		Py4a/b		Py6a/b
	Ccp				Ccp3		
	Mag					Mag2	
	Au				Au2		Au3
	Tbi				Tbi2		
	Ilm				Ilm1	Ilm2	
	Pl			Pl2		Pl3	
	Qz					Qz4	
	Ms					Ms2	
	Bt					Bt3	
	Kfs					Kfs3	
Intrusive Units	Grt					Grt	
	Apy				Apy		
	Py				Py4a	Py5	
	Ccp				Ccp3		
	Mag					Mag2	Au3
	Au				Au2		
	Mol						Mol

Figure 8. Mineral paragenesis for the Porky Main and Porky West deposits by geological unit. Three generations of gold occur: Au1 in the calc-silicate alteration of the mafic volcanic rock, Au2 in smoky quartz veins, and Au3 as remobilized gold in all units.

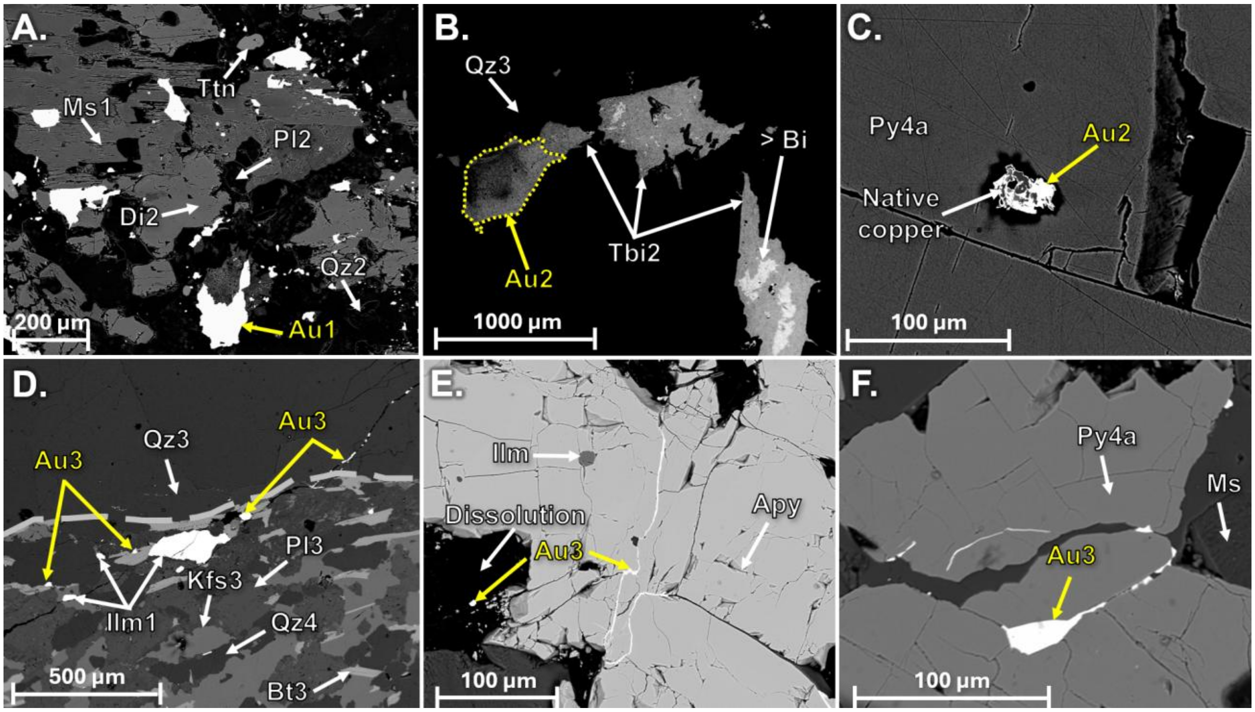

Figure 9. Backscattered electron images of the three gold phases. **A.** Visible Au1 in calc-silicate alteration of the mafic volcanic rocks and associated Ttn-Ms1-Di2-Pl2-Qz2. **B.** Visible Au2 with Tbi2 in V_2 vein. **C.** Au2 inclusion in Py4a. **D**. V_2 vein (top) and subarkosic unit (bottom) with Au3 forming in a fracture cutting both units. **E.** Remobilization of Au3 in Apy fractures with dissolution; ilmenite inclusions in Apy. **F.** Remobilization of Au3 in brecciated Py4a.

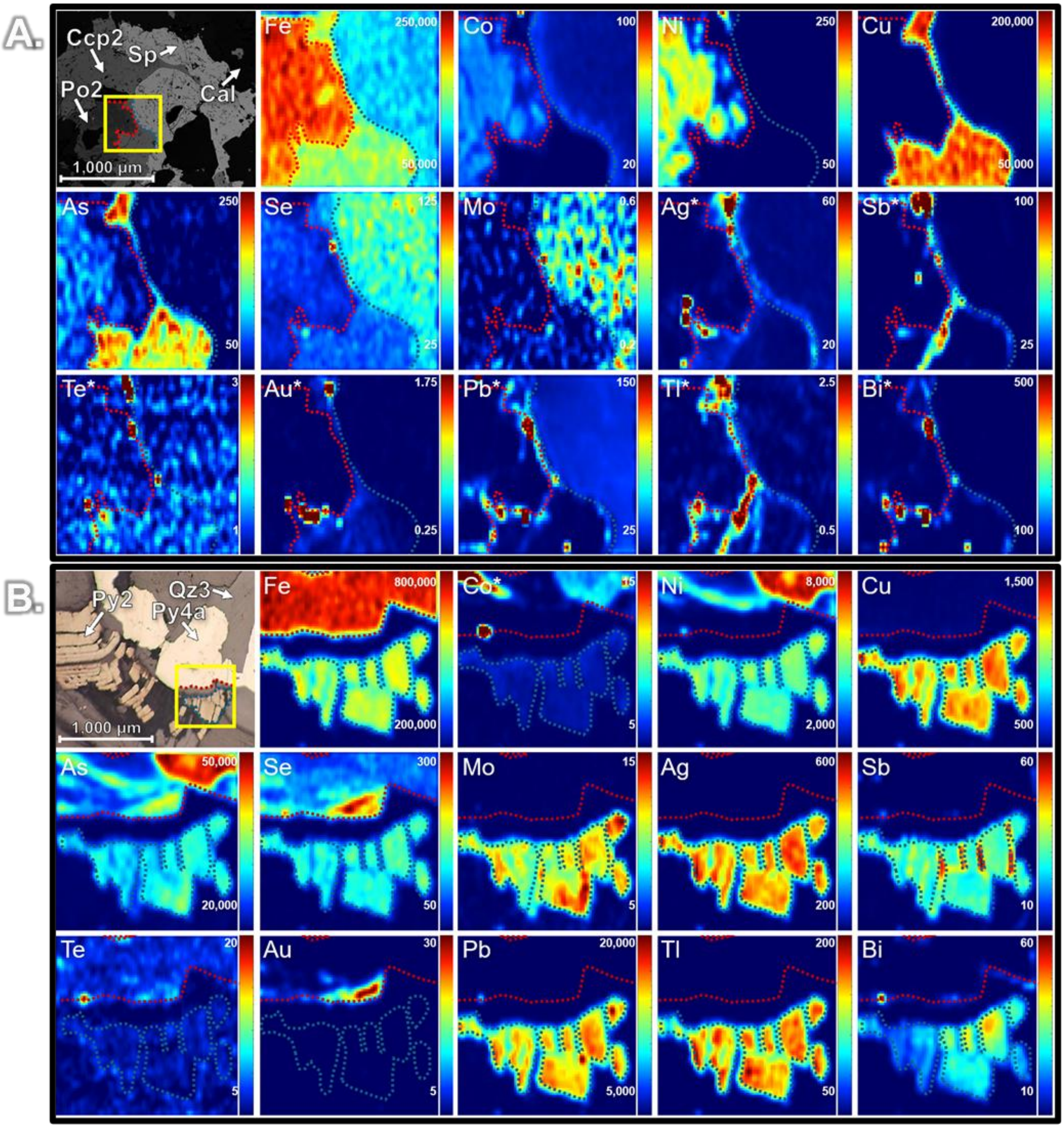

Figure 10. LA-ICP-MS semi-quantitative element maps. In Figures 10, 11, and 12, the yellow box correlates to the analyzed area. **A.** Po2/Ccp2/Sp and associated calc-silicate alteration with calcite as inclusions and matrix surrounding the grains where the Po2 is traced in red. Au has been liberated from the sulfide minerals and is now host in microfractures with corresponding Ag-Sb-Pb-Tl-Bi along the Po2-Ccp2 boundary. All concentrations are in ppm and elements with an * indicate maps displayed to the 99th percentile to reduce inclusions. In doing so, inclusions appear larger, but element concentration is better observed throughout the remaining sulfide

mineral. When ignoring the 99th percentile, the maximum values of these include Ag* = 612 ppm, Sb* = 2,325 ppm, Te* = 33 ppm, Au* = 6 ppm, Pb* = 5,262 ppm, Tl* = 10 ppm, and Bi* = 13,311 ppm. **B.** Colloform Py2, traced in blue, in a V_2 vein adjacent to Py4a, traced in red, in the subarkosic unit. This early pyrite generation is enriched in Ni-Cu-As-Se-Mo-Ag-Sb-Pb-Tl-Bi when compared to the Py4a, whereas Au is found in the crystal lattice in the Py4a with a Ni-As-Se association, where Co* = 75 ppm.

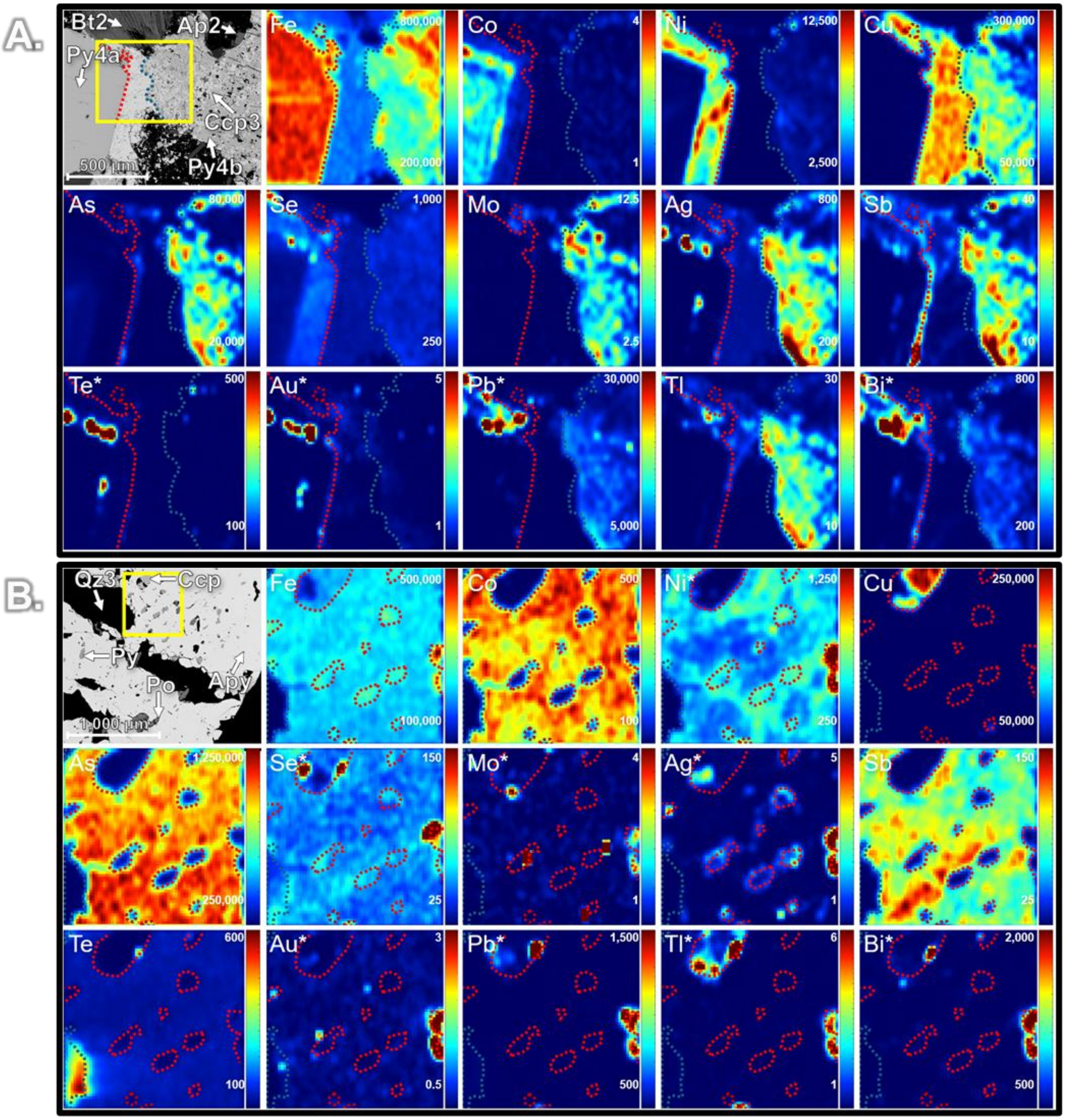

Figure 11. LA-ICP-MS semi-quantitative element maps. **A.** Euhedral Py4a, traced in red, and disseminated Py4b/Ccp3, with Py4b traced in blue, where Au occurs in the Co-Ni transition area with increased Se-Te-Pb-Bi in the Py4a. Au precipitation in the crystal lattice was associated with changing fluid conditions in the Co-Ni transition area with continued precipitation in the Ccp3/Py4b sulfide minerals. All concentrations are in ppm and elements with an * indicate maps displayed to the 99th percentile to reduce inclusions. Notable values include Te* = 1,484 ppm, Au* = 51 ppm, Pb* = 94,513 ppm, and Bi* = 3,683 ppm. **B.** Inclusion-rich Apy where the Po

Figures for Dixon et al.

inclusions are most favourable with Au with associated Ni-Ag-Pb-Tl-Bi. Inclusions have been traced in red. Notable values include Ni* = 3,191 ppm, Se* = 466 ppm, Mo* = 86 ppm, Ag* = 55 ppm, Au* = 12 ppm, Pb* = 43,679 ppm, Tl* = 139 ppm, and Bi* = 6,706 ppm.

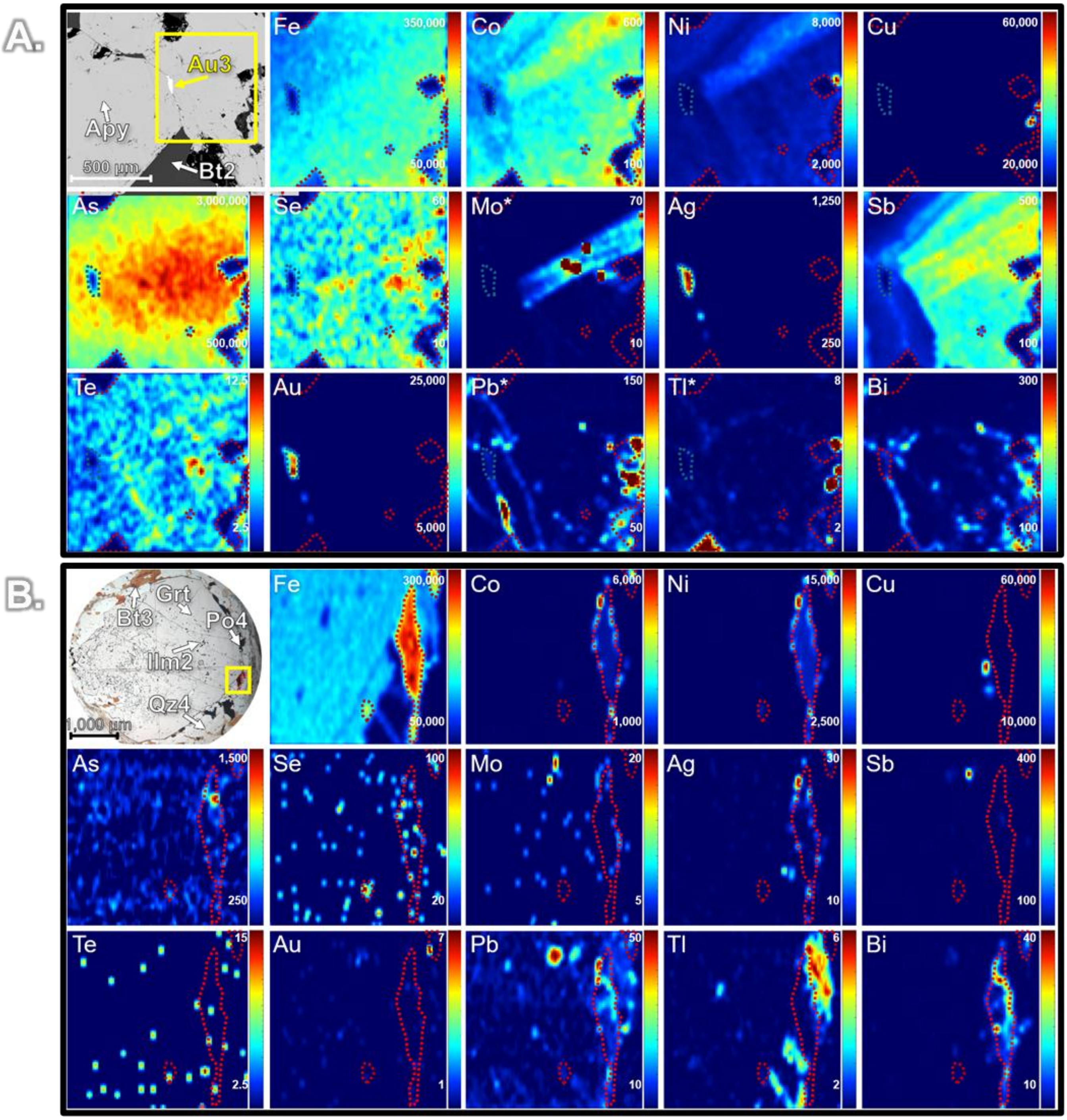

Figure 12. LA-ICP-MS semi-quantitative element maps. **A.** Remobilized Au in Apy with dissolution. In this sample, Au occurs in fractures with increased Ag-Pb-Tl-Bi. Zonation is evident with Fe-Co-Ni-As-Se-Mo-Sb-Te and suggests changing fluid conditions. Inclusions have been traced in red. All concentrations are in ppm and elements with an * indicate maps displayed to the 99th percentile to reduce inclusions. Notable values include Mo* = 589 ppm, Pb* = 962 ppm, and Tl* = 40 ppm. **B.** Po4, traced in red, forming around a garnet in the wacke unit with elevated Co-Ni and microfractures with Pb-Tl-Bi.

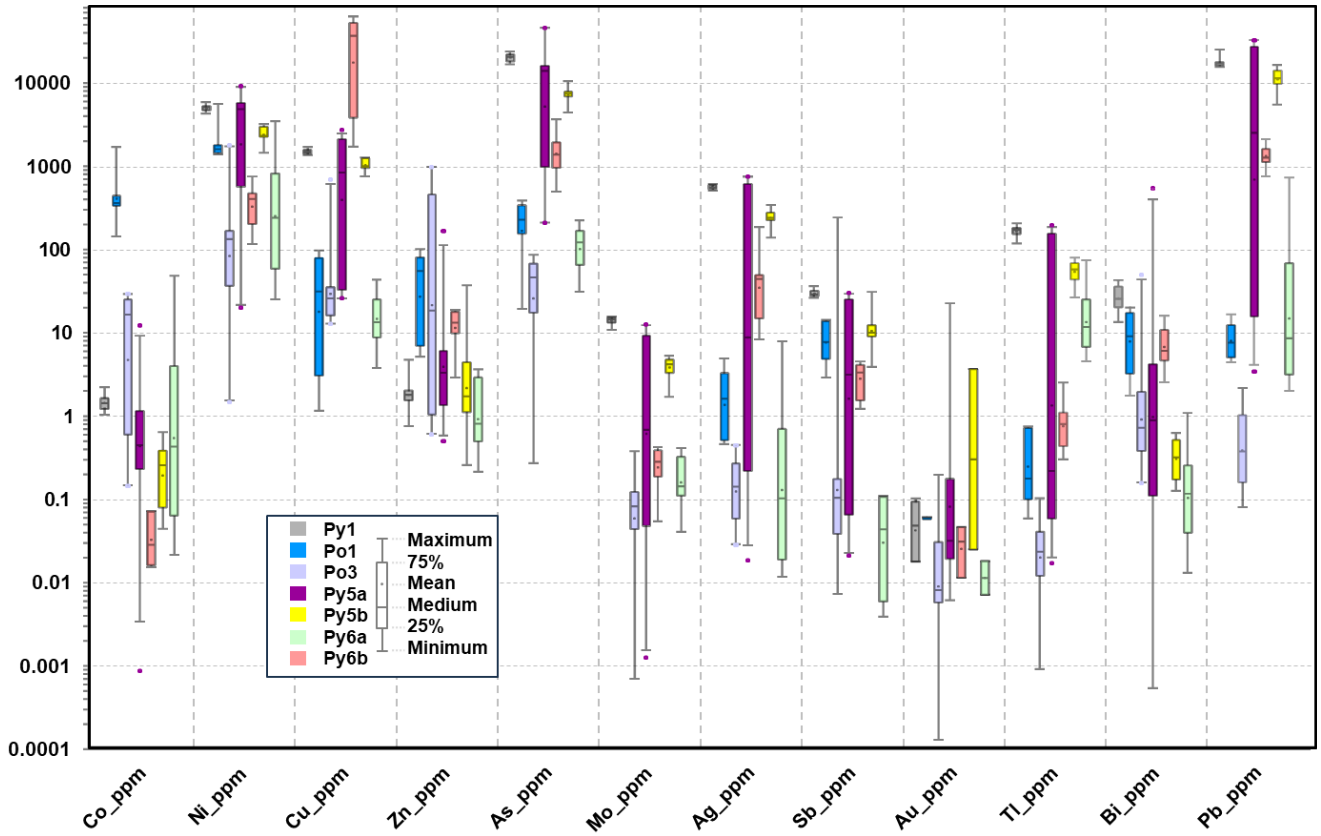

Figure 13. Tukey box and whisker plot of element concentrations in Py and Po generations. Py2 is an early colloform pyrite in the subarkose unit, Po2 is found in the calc-silicate alteration, Py4a/b are found in the V2 veins, Po4 is metamorphic associated, and Py6a/b are remobilized generations. Elements including Ni-Cu-Mo-Sb-Pb occur in greater abundance with Au-bearing sulfide minerals.

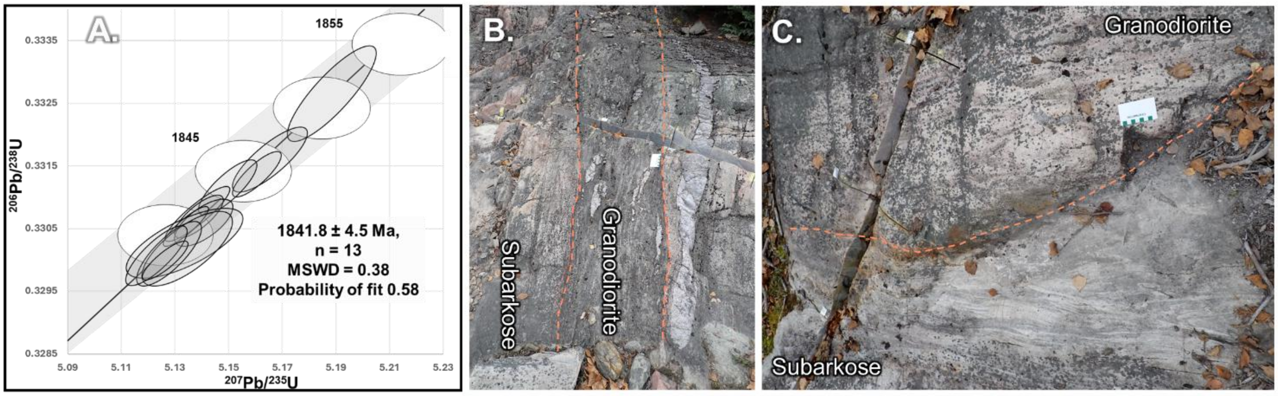

Figure 14 **A.** Zircon U-Pb geochronology of the granodiorite that intrudes the Porky Lake Group **B, C.** Outcrop photos showing granodiorite, traced, crosscutting the subarkosic unit.

Figures for Dixon et al.

Figure 15. Gold-related alteration and vein model of the Porky Main and Porky West deposits as related to the six stages of gold development as outlined in the text. **A.** *Stage 1.* Formation of V_1 veins in Assemblage A rocks and corresponding Po1-Py1-Ccp1. **B.** *Stage 2.* Juxtaposition of the Porky Lake Group, subsequent intrusive event, and formation of early colloform Py2. **C.** *Stage 3.* Calc-silicate alteration and introduction of visible Au with Po2-Ccp2-Sp. **D.** *Stage 4.* V_2 veins and the introduction of Apy-Py4a/b-Po3-Ccp3. Using empirical calculations of chlorite and biotite associated with this vein generation, these veins formed at ~315ºC and ~3.1 kbar or 10.2 km depth. **E.** *Stage 5.* Peak metamorphism during D_2 with Py5-Po4 aligned to foliation and subsequent folding of units during D_3. **F.** *Stage 6.* Remobilization of Au from earlier sulfide minerals and growth of the youngest pyrite forming Py6a/b and eventual exhumation and erosion to present day. The scale shown in **F** refers to the present position of the system at the present day but should not be used to infer depth in **A** to **E**, or in the development of the youngest sulfide minerals in **F**. The shapes of the various sulfide minerals are taken from thin sections and should only be treated as schematic representations of the sulfide mineral phases.